Anthropogenic and natural controls on atmospheric $\delta^{13}C$-CO_2 variations in the Yangtze River Delta: Insights from a carbon isotope modeling framework

Cheng Hu[1, 2*], Jiaping Xu[3], Cheng Liu[4], Yan Chen[3], Dong Yang[5], Wenjing Huang[2], Lichen Deng[6], Shoudong Liu[2], Timothy J. Griffis[7**], and Xuhui Lee[8]

[1] College of Biology and the Environment, Joint Center for sustainable Forestry in Southern China, Nanjing Forestry University, Nanjing, 210037, China

[2] Yale-NUIST Center on Atmospheric Environment, International Joint Laboratory on Climate and Environment Change (ILCEC), Nanjing University of Information, Science & Technology, Nanjing, 210044, China

[3] Jiangsu Climate Center, China Meteorological Administration, Nanjing, 210009, China

[4] Jiangxi Province Key Laboratory of the Causes and Control of Atmospheric Pollution, East China University of Technology, Nanchang, 330013, China

[5] Ningbo Meteorological Observatory, Ningbo, 315012, China

[6] Ecological Meteorology Center, Jiangxi Meteorological Bureau, Nanchang, 330096, China

[7] Department of Soil, Water, and Climate, University of Minnesota-Twin Cities, St. Paul, Minnesota, USA

[8] School of Forestry and Environmental Studies, Yale University, New Haven, Connecticut, USA

Correspondence:

*Cheng Hu, College of Biology and the Environment, Joint Center for sustainable Forestry in Southern China, Nanjing Forestry University, Nanjing, 210037, China. nihaohucheng@163.com or huxxx991@umn.edu

** Timothy J. Griffis, Department of Soil, Water, and Climate, University of Minnesota, St. Paul, MN 55108, timgriffis@umn.edu

To be submitted to *Atmospheric Chemistry and Physics*

Abstract:

The atmospheric carbon dioxide (CO_2) mixing ratio and its carbon isotope ($\boldsymbol{\delta}^{13}C\text{-}CO_2$) composition contain important CO_2 sink and source information spanning from ecosystem to global scales. The observation and simulation for both CO_2 and $\boldsymbol{\delta}^{13}C\text{-}CO_2$ can be used to constrain regional emissions and better understand the anthropogenic and natural mechanisms that control $\delta^{13}C\text{-}CO_2$ variations. Such work remains rare for urban environments, especially megacities. Here, we used near-continuous CO_2 and $\boldsymbol{\delta}^{13}C\text{-}CO_2$ measurements, from September 2013 to August 2015, and inverse modeling to constrain the CO_2 budget and investigate the main factors that dominated $\boldsymbol{\delta}^{13}C\text{-}CO_2$ variations for the Yangtze River Delta (YRD) region, one of the largest anthropogenic CO_2 hotspots and densely populated regions in China. We used the WRF-STILT model framework with category-specified EDGAR v4.3.2 CO_2 inventories to simulate hourly CO_2 mixing ratios and $\boldsymbol{\delta}^{13}C\text{-}CO_2$, evaluated these simulations with observations, and constrained the total anthropogenic CO_2 emission. We show that: (1) Top-down and bottom-up estimates of anthropogenic CO_2 emissions agreed well (bias < 6%) on an annual basis; (2) The WRF-STILT model can generally reproduce the observed diel and seasonal atmospheric $\boldsymbol{\delta}^{13}C\text{-}CO_2$ variations; (3) Anthropogenic CO_2 emissions played a much larger role than ecosystems in controlling the $\boldsymbol{\delta}^{13}C\text{-}CO_2$ seasonality. When excluding ecosystem respiration and photosynthetic discrimination in the YRD area, $\boldsymbol{\delta}^{13}C\text{-}CO_2$ seasonality increased from 1.53‰ to 1.66‰; (4) Atmospheric transport processes in summer amplified the cement CO_2 enhancement proportions in the YRD area, which dominated monthly $\boldsymbol{\delta}_s$ (the mixture of $\boldsymbol{\delta}^{13}C\text{-}CO_2$ from all regional end-members) variations. These findings support that the combination of long-term atmospheric carbon isotope observations and inverse modeling can provide a powerful constraint on the carbon cycle of these complex megacities.

Keywords: cements production, $^{13}C/^{12}C$ ratio, WRF-STILT model, plant photosynthetic discrimination

1. Introduction

Urban landscapes account for 70% of global CO_2 emissions and represent less than 3% of Earth's land area (Seto et al., 2014). Such CO_2 hotspots play a dominant role in controlling the rise in atmospheric CO_2 concentrations, which exceeded 412 ppm in December 2019 for global monthly average observations (https://www.esrl.noaa.gov/gmd/ccgg/trends/). Furthermore, the carbon isotope ratio of CO_2 (i.e. $\boldsymbol{\delta}^{13}C$ = $^{13}C/^{12}C$ ratio in delta notation) at the representative Mauna Loa site, USA, has steadily decreased to around -8.5‰, in December 2019 (https://www.esrl.noaa.gov/). Anthropogenic CO_2 emission is produced from fossil fuel burning and cement production. As the urban population is expected to increase by 2.5 to 6 billion people in 2050, anthropogenic CO_2 emissions are projected to increase dramatically, especially in developing regions and countries (Sargent et al., 2018; Ribeiro et al., 2019). Under such a scenario, the observations of atmospheric CO_2 and $\boldsymbol{\delta}^{13}C\text{-}CO_2$ in urban landscapes are of great importance to monitoring these potential CO_2 emissions hotspots (Lauvaux et al., 2016; Nathan et al., 2018; Graven et al., 2018; Pillai et al., 2016; Staufer et al., 2016).

Countries are required to report their CO_2 emissions according to the Intergovernmental Panel on Climate Change guidelines (IPCC, 2019), and many "bottom-up" methods have long been used to estimate CO_2 emissions worldwide, but such methods have high uncertainties for CO_2 emissions at regional (20%) to city (50 to 250%) scales (Gately & Hutyra, 2017; Gately et al., 2015). These large uncertainties are propagated into the estimation of biological fluxes in atmospheric inversions (Zhang et al., 2014; Jiang et al., 2014; Thompson et al., 2016). By using CO_2 observations, the "top-down" atmospheric inversion approach is a useful tool to evaluate "bottom-up" inventories (Graven et al., 2018; L. Hu et al., 2019; Lauvaux et al., 2016; Nathan et al., 2018). Previous research has shown that additional information, such as data on atmospheric $\boldsymbol{\Delta}^{14}CO_2\text{-}CO_2$, $\boldsymbol{\delta}^{13}C\text{-}CO_2$, and CO, is needed to better distinguish CO_2 emissions from different sources and to assess their uncertainties (Chen et al., 2017; Graven et al., 2018; Nathan et al., 2018; Cui et al., 2019). The use of hourly $\boldsymbol{\delta}^{13}C\text{-}CO_2$ observation in urban areas remains rare in inversion studies, yet such observations contain invaluable information of anthropogenic CO_2 from different categories.

Traditional estimates of $\boldsymbol{\delta}^{13}C\text{-}CO_2$ using isotope ratio mass spectrometry (IRMS) are very limited because flask air sample collection requires long preparation time and is expensive. Consequently, there is a lack of high temporal and long-term observations of $\boldsymbol{\delta}^{13}C\text{-}CO_2$ (Sturm et al., 2006). Isotope ratio infrared spectroscopy technology (IRIS) has overcome these limitations. As a result, *in situ* air sample analyses using IRIS analyzers are resulting in dense time series of $\boldsymbol{\delta}^{13}C\text{-}CO_2$. However, most of the established long-term IRMS and IRIS δ^{13}C-CO$_2$ measurement sites are representative of "background", natural, or agricultural ecosystems at locations far away from urban landscapes (Chen et al., 2017; Griffis, 2013).

To date, long-term (> 1 year) and continuous observations of both CO$_2$ and δ^{13}C-CO$_2$ have been reported for only five cities, including Bern, Switzerland (Sturm et al., 2006); Boston, USA (McManus et al., 2010); Salt Lake City, USA (Pataki et al., 2006); Beijing, China (Pang et al., 2016); and Nanjing, China (Xu et al., 2017). In these previous investigations, significant diel and seasonal variations of δ^{13}C-CO$_2$ have been observed; these patterns were modulated by fossil fuel combustion, plant respiration and photosynthesis, and changes in the height of the atmospheric boundary layer (Sturm et al., 2006; Guha and Ghosh, 2010). No study has quantified the impact of each factor on the seasonal variation of δ^{13}C-CO$_2$. This represents an important knowledge gap in understanding the underlying mechanisms of carbon cycling in complex urban ecosystems.

The traditional δ^{13}C-CO$_2$ isotope partitioning methods (including Miller-Tans and the Keeling plot approaches) have been used to constrain different CO$_2$ sources worldwide (Keeling, 1960; Vardag et al., 2015; Newman et al., 2016; Pang et al., 2016; Xu et al., 2017). These methods are based on the assumption that partitioned atmospheric CO$_2$ enhancement components from different sources can represent CO$_2$ emissions at the "target area" (Miller and Tans, 2003; Ballantyne et al., 2011). Carbon dioxide emissions are highly inhomogeneous at the urban scale, with extremely strong point/line sources, and the final partitioning results are highly uncertain without considerations of source footprint characteristics (Gately & Hutyra, 2017; Cui et al., 2019; Martin et al., 2019). Atmospheric transport models can help to resolve such problems, and the coupling of atmospheric transport models with isotope observations have recently been applied in global and regional CO$_2$ partitioning studies (Chen et al., 2017; Cui et al., 2019; Graven et al., 2018; C. Hu et al., 2018b). Although urban CO$_2$ inversions have been applied successfully in several studies in Europe and the United States (Bréon et al., 2015; Turnbull et al., 2015; Pillai et al., 2016; Brioude et al., 2013; Turner et al., 2016), urban CO$_2$ inversions in China are rare (Berezin et al., 2013; C. Hu, 2018a; Worden et al., 2012), presumably because of the scarcity of high quality δ^{13}C-CO$_2$ and CO$_2$ observations.

The Yangtze River Delta (YRD) ranks as one of the most densely populated regions in the world and is an important anthropogenic CO$_2$ hotspot. Major anthropogenic sources include the power industry, oil refineries/transformation and cement production. Having the largest source of cement-derived CO$_2$ production across China and the world (Cai et al., 2015), the YRD contributed 20% of national cement production, nearly 12% of world's total cement output in 2014 (USGS, 2014; Xu et al., 2017; Yang et al., 2017). In addition to anthropogenic factors, natural ecosystems and croplands act as significant CO$_2$ sinks and sources within the YRD. Independent quantification of the fossil and cement CO$_2$ emission and assessment of their impact on atmospheric $\boldsymbol{\delta}^{13}$C-CO$_2$ have potential to improve our understanding of urban CO$_2$ cycling. Further, the observations and simulations of both atmospheric CO$_2$ and $\boldsymbol{\delta}^{13}$C-CO$_2$ can help us relate atmospheric CO$_2$ dynamics with future emission control strategies.

Here, we combine long-term (>2 years) CO$_2$ and $\boldsymbol{\delta}^{13}$C-CO$_2$ observations with atmospheric transport model simulations to study urban atmospheric CO$_2$ and $\boldsymbol{\delta}^{13}$C-CO$_2$ variations. The objectives were to: (1) Constrain anthropogenic CO$_2$ emissions and determine the main sources of uncertainty for $\boldsymbol{\delta}^{13}$C-CO$_2$ simulations, and (2) Quantify the relative contributions of each factor (i.e. background, anthropogenic CO$_2$ emissions especially for cement production, ecosystem photosynthesis and respiration) to seasonal variations of atmospheric $\boldsymbol{\delta}^{13}$C-CO$_2$.

2. Materials and methods

2.1 Observations of atmospheric CO$_2$ mixing ratio, $\boldsymbol{\delta}^{13}$C-CO$_2$ and supporting variables

The observation site is located on the Nanjing University of Information Science and Technology campus (hereafter NUIST, 32°12'N, 118°43'E, green dot in Figure 1a). Continuous atmospheric CO$_2$ mixing ratios and $\boldsymbol{\delta}^{13}$C-CO$_2$ were measured at a height of 34 m above ground with an IRIS analyzer (model G1101-i, Picarro Inc., Sunnyvale, CA). The observation period extended from September 2013 to August 2015. Calibrations for CO$_2$ mixing ratio and $\boldsymbol{\delta}^{13}$C-CO$_2$ were conducted with standard gases traceable to NOAA/GML (NOAA Global Monitoring Laboratory) standards. Calibration details are provided by Xu et al. (2017). Based on Allan variance analyses, the hourly precisions of CO$_2$ and $\boldsymbol{\delta}^{13}$C-CO$_2$ were 0.07 ppm and 0.05‰, respectively. We note that the $\boldsymbol{\delta}^{13}$C-CO$_2$ IRIS (model G1101-i) measurements are sensitive to water vapor concentration. Sensitivity tests reveal that the $\boldsymbol{\delta}^{13}$C-CO$_2$ IRIS measurements are biased high (less than 0.74‰) when water vapor mole fraction exceeds 2%. The data presented here have been corrected following the procedures outlined in Xu et al. (2017).

We separated the two-year study period into seasons (autumn: September, October, November; winter: December, January, February; spring: March, April, May; summer: June, July, August). Further, for an annual comparison, we examined the period from September 2013 to August 2014 (Year 2014) versus September 2014 to August 2015 (Year 2015).

The YRD is a cement production hotspot in China (Figure 1b). It had a total population of 190 million in 2018 (Figure 2a) with 24.2 million in the city of Shanghai, 9.8 million in Hangzhou city (provincial capital of Zhejiang), 8.4 million in Nanjing city (provincial capital of Jiangsu), and 8.1 million in Hefei city (provincial capital of Anhui). The CO$_2$ related production data (i.e. cement) and energy consumption data (i.e. coal and natural gas) were obtained from local official sources using the same method described in Shen et al. (2014).

To examine the effects of plant photosynthesis on atmospheric CO_2 variations, we used NDVI (Normalized Difference Vegetation Index), SIF (solar-induced chlorophyll fluorescence) and GPP (gross primary productivity) information. These three products have a global distribution with spatial resolution of 0.05^{o} by 0.05^{o}. The NDVI has a temporal resolution of 16 days and SIF and GPP products have a temporal resolution of 8 days (Li & Xiao, 2019; http://globalecology.unh.edu/data/). Land-use and land-cover classification in Yangtze River Delta for 2014 was applied by using NDVI data from MOD13A2.

2.2 Simulation of atmospheric $\boldsymbol{\delta}^{13}$C-CO_2

2.2.1 General equations

The simulation of atmospheric $\boldsymbol{\delta}^{13}$C-CO_2 is based on mass conservation. First, we briefly describe the simulation of atmospheric CO_2 mixing ratios (more details are provided in Section 2.2.2), following the previous work of Hu et al., (2018b), where atmospheric CO_2 was simulated (CO_{2_sim}) as the sum of background (CO_{2_bg}) and the contribution from all regional sources/sinks ($[\boldsymbol{\Delta}CO_{2\_sim}]_i$), as

$$CO_{2\_sim} = CO_{2\_bg} + \sum_{i=1}^{n} [\Delta CO_{2\_sim}]_i \qquad (1)$$

Note that $\boldsymbol{\Delta}CO_2$ is the sum of all simulated sources/sinks $[\boldsymbol{\Delta}CO_{2\_sim}]_i$ and represents the total simulated CO_2 enhancement. We use $\boldsymbol{\Delta}CO_{2\_obs}$ as the observed CO_2 total enhancement, which can be calculated by using the CO_2 observation minus the CO_2 background values. Based on mass conservation, we estimated the $^{13}CO_2$ composition by multiplying the left- and right-hand sides of equation (1) by $\boldsymbol{\delta}^{13}$C,

$$\delta^{13}C_{a\_sim} = \frac{\delta^{13}C_{bg} \times CO_{2\_bg} + \sum_{i=1}^{n} \delta_i^{13} \times [\Delta CO_{2\_sim}]_i}{CO_{2\_sim}} \qquad (2)$$

where $\boldsymbol{\delta}^{13}C_{a\_sim}$ and $\boldsymbol{\delta}^{13}C_{bg}$ represent the simulated atmospheric $\boldsymbol{\delta}^{13}$C-CO_2 and background $\boldsymbol{\delta}^{13}CO_2$, $\boldsymbol{\delta}_i^{13}$ is the $\boldsymbol{\delta}^{13}$C-CO_2 for end-member *i* (including anthropogenic and biological source categories). The $\boldsymbol{\delta}^{13}$C-CO_2 contributions from all regional sources/sinks can be further reformatted as equation 3,

$$\sum_{i=1}^{n} \delta_i^{13} \times [\Delta CO_{2\_sim}]_i = \delta_{s\_sim} \times \sum_{i=1}^{n} [\Delta CO_{2\_sim}]_i \qquad (3)$$

where $\boldsymbol{\delta}_{s\_sim}$ is the simulated enhancement-weighted mean of all regional end-members. We use $\boldsymbol{\delta}_s$ as the observed term to distinguish it from $\boldsymbol{\delta}_{s\_sim}$ (Newman et al., 2008), which will be described in detail in section 2.2.5. The product on the right-hand side of equation 3 is the simulated regional source term that is added to the background value and contains both enhancement and $\boldsymbol{\delta}^{13}$C-CO_2 signals contributed by different CO_2 sources/sinks. This product can also be treated as an observed term when using the derived $\boldsymbol{\delta}_{s\_obs}$ and observed $\boldsymbol{\Delta}CO_{2\_obs}$ values.

To date, there are no available global $\boldsymbol{\delta}^{13}$C-CO_2 background products and the choice of $\boldsymbol{\delta}^{13}C_{bg}$ is essential to simulating $\boldsymbol{\delta}^{13}C_a$. Here, we apply three strategies. First, we used discrete $\boldsymbol{\delta}^{13}$C-CO_2 flask observations at Mount Waliguan (hereafter WLG, 36°17'N, 100°54'E; https://www.esrl.noaa.gov/gmd/dv/data/) to represent the $\boldsymbol{\delta}^{13}$C-CO_2 background signal at our site. These observations were measured at weekly intervals to the end of 2015. A digital filtering curve fitting (CCGCRV) regression method was applied to derive hourly background values following Thoning et al. (1989). There are, however, reasons why WLG may not be an ideal background site for our study domain. For example, based on the previous simulation results for the CO_2 background sources, most of the back trajectories originate from the free atmosphere or 1000 m higher above the ground (Hu et al., 2019). Further, the footprint at the north/west edge of Domain 1 is relatively small, indicating that most back trajectories were observed above the planetary boundary layer height (hereafter PBLH). Here, the WLG observations were made near the surface. Further, WLG is not located at the border of our simulation domain 1. Therefore, the strong vertical $\boldsymbol{\delta}^{13}$C-CO_2 gradients between the boundary layer and the free tropospheric atmosphere (Chen et al., 2006; Guha et al., 2010; Sturm et al., 2013) can cause a low bias in the $\boldsymbol{\delta}^{13}$C-CO_2 background when using this approach.

In the second approach, the $\boldsymbol{\delta}^{13}$C-CO_2 background signal was estimated with wintertime "clean" air CO_2 and $\boldsymbol{\delta}^{13}$C-CO_2 observations at the NUIST site, using the following equation

$$\delta^{13}C_{bg} = \frac{\delta^{13}C_a \times CO_2 - \sum_{i=1}^{n} \delta_i^{13} \times [\Delta CO_{2\_sim}]_i}{CO_{2\_bg}} \qquad (4)$$

where $\boldsymbol{\delta}^{13}C_a$ and CO_2 represent atmospheric $\boldsymbol{\delta}^{13}$C-CO_2 and CO_2 observations at the NUIST site under clean conditions. Note that $\boldsymbol{\delta}^{13}C_a$ represents the observed $\boldsymbol{\delta}^{13}$C-CO_2 not the simulated $\boldsymbol{\delta}^{13}$C-CO_2 ($\boldsymbol{\delta}^{13}C_{a\_sim}$) as shown in equation 2. $[\boldsymbol{\Delta}CO_{2\_sim}]_i$ is the simulated category-specified CO_2 enhancements. We defined clean conditions as the bottom 5% wintertime CO_2 observations to minimize simulated CO_2 enhancement errors from both biological and anthropogenic CO_2 simulations on $\boldsymbol{\delta}^{13}$C-CO_2 background calculation. The CO_{2_bg} is obtained from heights 1000 m above ground level (see Section 2.2.3).

In the third approach, we avoid the use of modeled $[\boldsymbol{\Delta}CO_{2\_sim}]_i$ results and replaced the simulated regional source term in equation 4 with observed $\boldsymbol{\delta}_{s\_obs} \times \boldsymbol{\Delta}CO_{2\_obs}$, as described in equation 3, and used the Miller-

Tans regression method to calculate monthly $\boldsymbol{\delta}_{s\_obs}$. This approach does not require simulation of $[\Delta CO_2]_i$ or the corresponding $\boldsymbol{\delta}^{13}C$-$CO_2$ signals. The hourly $\boldsymbol{\delta}^{13}C$-$CO_2$ background value can be derived by using $\boldsymbol{\delta}_{s\_obs}$, CO_2 background, observed atmospheric $\boldsymbol{\delta}^{13}C_a$ and CO_2 (see details in Section 2.3 and supplement materials). Comparison of these three strategies will be evaluated and discussed in Section 3.2.1. Similar methods used to derive other background tracers have included CO_2 (Alden et al., 2016; Verhulst et al., 2017), CO (Wang et al., 2010; Ruckstuhl et al., 2012) and CH_4 (Zhao et al., 2009; Verhulst et al., 2017; Hu et al., 2019). To analyze the controlling factors for the $\boldsymbol{\delta}^{13}C$-$CO_2$ seasonality, the CCGCRV (a digital filtering curve fitting program developed by the Carbon Cycle Group, NOAA, USA) regression was applied to the background, observations, and simulations. Finally, we derived CCGCRV curve fitting lines by using 11 regressed parameters, which were based on the hourly time series of observations/simulations, and defined the difference between peak and trough in one year as the seasonality of $\boldsymbol{\delta}^{13}C$-$CO_2$.

2.2.2 Simulation of atmospheric CO_2 mixing ratios

In equation 1, the CO_{2_bg} is obtained from the Carbon Tracker 2016 product, which provides global CO_2 distributions from the ground level up to a height of 50 km. We used the averaged concentration above the latitude and longitude where the released particles entered the study domain 1 (Figure 1a). The variable ΔCO_{2_sim} was derived by multiplying the simulated hourly footprint function with the hourly CO_2 fluxes (Hu et al., 2018a; b). Considering the diurnal variations of both anthropogenic and biological CO_2 fluxes, 168 footprints were obtained representing each simulated hour. This accounted for the back trajectory of particle movement for 168 hours (i.e. 24 hours per day for 7 days) of transport. The 168 footprints are multiplied by the corresponding hourly CO_2 flux. The CO_2 fluxes contain anthropogenic CO_2 emissions, biological CO_2 flux and biomass burning. Here the anthropogenic CO_2 emission sources include power industry, combustion for manufacturing, non-metallic minerals production (cement), oil refineries/transformation industry, energy for building and road transportation. Theoretically, ΔCO_{2_sim} represents the CO_2 changes contributed by every pixel within the simulated domain. As shown by Hu et al. (2018a), most of the ΔCO_{2_sim} is contributed by sink/source activity within the YRD area. In order to quantify the relative contributions within the YRD area, we separated the study domain into 5 zones based on provincial administrative boundaries including Jiangsu, Anhui, Zhejiang, Shanghai, and the remaining area outside the YRD (Figure 2). The modeled CO_2 was calculated as follows:

$$\Delta CO_{2\_sim} = \sum_{i=1}^{168} flux_i \times footprint_i \qquad (5)$$

where $flux_i$ (units: mol m^{-2} s^{-1}) corresponds to each CO_2 flux category simulated for each domain for a specific hour *i*, and footprint (units: ppm m^2 s/μmol) is the model simulated sensitivity of observed CO_2 enhancement to flux changes in each pixel. The *i* contains the hourly footprint during trajectory of particle movement for 168 hours as described above. The CO_2 enhancement from each of the 5 zones were simulated by multiplying CO_2 emissions in each province with the corresponding footprint.

2.2.3 WRF-STILT model configuration

The Stochastic Time-Inverted Lagrangian Transport (hereafter STILT) model was used to generate the above footprint, which is defined as the sensitivity of atmospheric CO_2 enhancement to the upwind flux at the receptor site (observation site). The meteorological fields used to drive the STILT model were simulated with the Weather Research and Forecasting Model (WRF3.5) at high spatial and temporal resolutions. The innermost nested domain (D3, 3 km × 3 km, Figure 1) contains the YRD area, where the most sensitive footprint is located, and the intermediate domain (D2, 9 km × 9 km) and outermost (D1, 27 km × 27 km) represent Eastern China and Central and Eastern China, respectively. The same physical schemes and parameter setup for the WRF meteorological fields simulation and the Domain in the STILT model have been used previously for inverse analyses (Hu et al., 2019). These previous studies at the NUIST observation site have shown very good performance in simulating the meteorological fields, which is essential for reliable STILT simulations. The hourly footprint was simulated by releasing 500 particles from the NUIST measurement site and tracking their backward locations every 5 minutes for a period of 7 days. Particle numbers and their residence time within half of the PBLH were used to calculate the footprint over the 7 day period. For the CO_2 background of each hour, we tracked the sources of air particles back trajectory for 7 days, and defined these CO_2 mixing ratios in Carbon Tracker as the hourly CO_2 background values (Peters et al., 2007).

2.2.4 A priori anthropogenic CO_2 emissions and net ecosystem exchange

The Emission Database for Global Atmospheric Research (EDGAR v4.3.2) inventory was selected as the *a priori* anthropogenic CO_2 emissions (Figure 2a), which is based on the International Energy Agency's (IEA) energy budget statistics and provides detailed CO_2 source maps (29 categories, including both organic and fossil emissions, IEA, 2012) with global coverage at high spatial resolution ($0.1^o \times 0.1^o$). The EDGAR CO_2 emissions are the most up-to-date global inventory with sectoral detail (Janssens-Maenhout et al., 2017; Schneising et al., 2013). Other inventories, including the Fossil Fuel Data Assimilation System (FFDAS, Rayner et al., 2010) and the Open-source Data Inventory for Anthropogenic CO_2 (ODIAC, Oda et al., 2018) also provide global CO_2 emissions. However, these inventories only provide total CO_2 emissions or have very limited emission categories, which limit our ability to provide isotope end-member information. EDGAR v4.3.2 provides emission estimates at a monthly time scale. Here, we applied hourly scaling factors for different categories following Hu et al., (2018a). EDGAR v4.3.2 with monthly resolution is available only for 2010. We assume that each CO_2 category changes linearly from its 2010 value (Peters et al., 2007) and apply an annual scaling factor of 1.145 to derive CO_2 emissions for 2014 and 2015. This scaling factor is based on Carbon Tracker, dividing the same anthropogenic CO_2 emissions for YRD in years 2014-2015 by that in 2010.

The biological flux or net ecosystem CO_2 exchange (NEE) and biomass burning CO_2 emissions come from Carbon Tracker *a posteriori* flux at 3-hour intervals and at a spatial resolution of $1^{o} \times 1^{o}$. Because NEE is much smaller than the anthropogenic CO_2 emissions in such densely developed urban landscapes, we homogeneously distributed this flux at a spatial resolution of 0.1^{o} within each grid to match the footprint.

2.2.5 Simulation of the carbon isotope ratio of all sources ($\boldsymbol{\delta}_{s\_sim}$)

The carbon isotope ratio of all the surface sources was calculated as (Newman et al., 2008):

$$\sum_{i=1}^{n} \delta_i \times p_i = \delta_{s\_sim} \tag{6}$$

where δ_i is the $\boldsymbol{\delta}^{13}C\text{-}CO_2$ value from source category *i*, and p_i is the corresponding enhancement proportion (i.e. proportions of a specific enhancement *i* to total CO_2 enhancement). We define $\boldsymbol{\delta}_{s\_sim}$ as the simulated carbon isotope ratio of all sources to differentiate it from the observed $\boldsymbol{\delta}_{s\_obs}$. Based on fossil fuel usage characteristics in YRD, we reassigned the EDGAR v4.3.2 categories according to fuel types. Coal was the fuel type for manufacturing, oil for oil refinery, natural gas for buildings, and diesel and gasoline for transportation. The power industry consumed 5% natural gas and 95% coal based on local activity data in YRD (China statistical Yearbook, 2015). The non-metallic mineral production was mainly for cement. Since there is a lack of detailed information for non-metallic mineral production, we simply attributed 100% of it to cement production. Chemical processes were mainly ammonia synthesis. Based on a literature review and our previous work (Xu et al., 2017), typical $\boldsymbol{\delta}^{13}C\text{-}CO_2$ values for natural gas (−39.06‰ ± 1.07‰), coal (−25.46‰ ± 0.39‰), fuel oil (−29.32‰ ± 0.15‰), gasoline (−28.69‰ ± 0.50‰), ammonia synthesis (−28.18‰ ± 0.55‰), and diesel (−28.93‰ ± 0.26‰), pig iron (−24.90‰ ± 0.40‰), crude steel (−25.28‰ ± 0.40‰), cement (0‰ ± 0.30‰), biofuel combustion and biological emissions (−28.20‰ ± 1.00‰) were used in this study. We also applied a value of −28.20‰ for photosynthesis (Griffis et al., 2008; Lai et al., 2014) because YRD is a region dominated by C_3 plants. Since CO_2 emissions associated with human respiration (Prairie and Duarte, 2017; Turnbull et al., 2015;

Miller et al., 2020) are relatively small (3.7% of anthropogenic emissions in the YRD area, Xu et al., 2017), and given that the local food diet is dominated by C_3 grains that have a similar $\boldsymbol{\delta}^{13}C\text{-}CO_2$ value as the biological CO_2 flux of −28.20‰, we assume it has the same isotope signals as local C_3 plants and ecosystem respiration. Further, the biological CO_2 flux from the Carbon Tracker assimilation system considered anthropogenic as fixed and attributed the remainder to the biological CO_2 flux (Peters et al., 2007). Consequently, we believe the uncertainty in the biological CO_2 flux will include the small proportion of human respiration.

To evaluate the simulated $\boldsymbol{\delta}_{s\_sim}$, we applied the Miller-Tans and Keeling plot approaches to derive $\boldsymbol{\delta}_{s\_obs}$ from the observed concentration and atmospheric $^{13}CO_2$-CO_2 (Xu et al. 2017). We then used the results to evaluate the calculations made with Equation (6).

2.3 Independent IPCC method for anthropogenic CO_2 emissions

Large differences among inventories have been previously found even for the same region (Berezin et al., 2013; Andrew, 2019). For comparison with the EDGAR v4.3.2 inventory results, we derived the anthropogenic CO_2 emissions by using an independent IPCC method. Here, we illustrate the calculation for cement CO_2 emissions. Note that the IPCC only recommended an EF for clinker, which is an intermediate product of cement. To calculate cement CO_2 emissions, we need to calculate it based on clinker production, as shown in Equation (7),

$$CO_2[cement] = M_{cement} \times C_{clinker} \times EF_{clinker} \tag{7}$$

where CO_2[cement] is the chemical process CO_2 emissions for cement production, M_{cement} is the production of cement, $C_{clinker}$ represents the clinker to cement ratio (%), and $EF_{clinker}$ is the CO_2 emission factor for clinker production. The IPCC recommended an $EF_{clinker}$ value of 0.52 ± 0.01 tonne CO_2 per tonne clinker produced, where CaO content for clinker is assumed to be 65% with 100% CaO from calcium carbonate material (IPCC 2013). The EF appears to be well constrained, showing little variation among provinces with mean values ranging from 0.512 to 0.525 (Yang et al., 2017). For the $C_{clinker}$ values, it generally showed a decreasing trend from 64.5% in 2004 to 56.9% in 2015 for all of China (Figure S1), with an average value of 57.0% during 2014 and 2015.

2.4 Multiplicative scaling factor method

To quantify anthropogenic CO_2 emissions and to compare them with EDGAR products, we first derived the monthly scaling factors for anthropogenic CO_2 emissions using a multiplicative scaling factor (hereafter MSF) method (Sargent et al., 2018; He et al., 2020), and then obtained annual averages. The monthly scaling factors (SFs) were calculated as:

$$MSF = \frac{CO_{2\_obs} - CO_{2\_bg} - \Delta CO_{2\_bio} - \Delta CO_{2\_fire}}{\Delta CO_{2\_anthro}} \qquad (8)$$

where CO_{2_obs}, ΔCO_{2_bio}, ΔCO_{2_fire} and ΔCO_{2_anthro} represent observed CO_2 mixing ratios, simulated CO_2 enhancements contributed by biological flux, biomass burning, and anthropogenic emissions, respectively. Uncertainties of all factors on the final MSFs were calculated based on Monte Carlo methods, where the normal sample probability distribution was applied and the upper 97.5% and lower 2.5% of the values was considered as the uncertainty for MSF (Cao et al., 2016).

3. Results and Discussion

3.1 Evaluation of hourly CO_2 mixing ratios

3.1.1 Hourly and monthly CO_2 mixing ratio comparisons

This section examines the general performance of simulating hourly CO_2 mixing ratios. The two-year average hourly footprint is shown in Figure 2b where the source area (blue-red) indicates strong sensitivity of the CO_2 observations to regional sources. This footprint shape is representative of the YRD area. To quantify the relative contributions from each province, we calculated CO_2 enhancements contributed by Anhui, Jiangsu, Zhejiang, Shanghai, and the remaining area outside of the YRD, respectively. The results indicate that Jiangsu contributed approximately 80% of the total enhancement (discussed further in Section 3.1.2). Comparisons between simulated and observed hourly CO_2 mixing ratios are displayed in Figure 3a for both years. For all hourly data in each year, the model versus observation correlation coefficient (R) was $R = 0.38$ ($n = 8204$, $P < 0.001$) and RMSE = 29.44 ppm for 2014, and $R = 0.35$ ($n = 7262$, $P < 0.001$) and RMSE = 30.22 ppm for 2015. These results indicate that the model can simulate the synoptic and diel CO_2 variations over the two-year period. The model also captured the monthly and seasonal variations of CO_2 mixing ratios (daily averages are shown in Figure S2). The simulations captured the trend of rising CO_2 mixing ratios after October and the drawdown of CO_2 to the background value during the summer.

Figures 3b-d illustrate the average monthly daily, nighttime (22:00-06:00, local time), and daytime (10:00-16:00) CO_2 mixing ratios. These monthly values contain the effects of atmospheric transport, background and variations in CO_2 emissions. The observed and simulated CO_2 mixing ratios showed a significant increase from September 2013 to January 2014. Here, the CO_2 mixing ratios increased by 16.0 ppm according to the model results and 17.2 ppm according to the observations. The background values increased by 8.1 ppm and accounted for 47% of the total CO_2 increase, and the net CO_2 flux (*a priori*) for YRD increased by 15%. We attributed the remaining 38% increase to changes in atmospheric transport processes including lower PBLH in January 2014 than in September 2013. To quantify how variations in

PBLH affected CO_2 mixing ratios, we compared the simulated monthly anthropogenic CO_2 enhancement differences in the same months of different years, to eliminate the influence of monthly emission variations on CO_2 enhancements. Twelve monthly paired values were used and are shown in Figure 4. This analysis indicates that atmospheric CO_2 mixing ratios decreased by about 3.7 ppm for an increase of PBLH by 100 m. We also note that there were two months (March and August) that fall far below this trend, implying that changes in the monthly footprints (source area) can also play an important role.

On an annual timescale, the simulated average CO_2 mixing ratios were 436.63 ppm and 437.11 ppm for 2014 and 2015, respectively. Since the anthropogenic CO_2 emissions used in the model are the same for both years, the simulated annual average CO_2 difference can be used to quantify the influence associated with meteorological factors and ecosystem carbon cycling. Between these two years, the CO_2 background increased by 1.78 ppm, the biological enhancement decreased by 1.04 ppm from 2014 to 2015. The remaining 0.26 ppm change between 2014 and 2015 indicates a relatively small meteorological effect for the annual averages, such as a slight change in dominant wind direction or a PBLH difference.

The simulated annual average NEE CO_2 enhancements were 2.64 ppm and 1.60 ppm for the respective years. For comparison, the annual average anthropogenic enhancements were 36.20 ppm and 34.90 ppm for 2014 and 2015, respectively. The monthly NEE enhancement varied from -0.1 ppm in May 2015 to +6.0 ppm July 2014, indicating NEE contributes positively for enhancement in most months (Figure 5a), even though the sign of monthly averaged NEE flux in summer was negative (sinks). This positive contribution was mainly caused by diel PBLH variations between daytime (smaller negative enhancement) and nighttime (larger positive enhancement). To further evaluate the impact of plant photosynthetic activity on the regional CO_2 cycle, we examined the NDVI, SIF and GPP seasonal patterns (Figures 5d-f). These three datasets revealed two peaks during each year, which is related to increased photosynthetic activity. The first peak occurred in May and the second in August-September, corresponding to the growing season of wheat and corn/rice, respectively (Deng et al., 2015). We note that GPP was derived from SIF, and as a result, they share a similar seasonal cycle. The land-use classification in YRD for 2014 (Figure S3) shows that north YRD is dominated by agricultural land and south dominated by forest land, and our observation site was more surrounded by agricultural land which corresponded well with observed NDVI, SIF and GPP seasonal patterns. The peak SIF and GPP signals during the summer were about 20 times greater than during the winter. Consequently, we can ignore the potential influence of photosynthetic activity on the regional CO_2 enhancements during the non-growing seasons.

3.1.2 Components of urban CO_2 enhancement

Here, we diagnose the source contributions to the urban CO_2 enhancement. The observed anthropogenic CO_2 enhancements, which were derived by subtracting CO_2 background and simulated biological enhancement from CO_2 concentration observations, were 38.36±3.32 ppm and 37.89±2.80 ppm for 2014 and 2015, respectively. Here, the uncertainty of the observed anthropogenic CO_2 enhancements was calculated by prescribing a 2 ppm potential bias for the Carbon Tracker CO_2 fields and 50% to the simulated biological CO_2 enhancement (Hu et al., 2018b). The corresponding simulated anthropogenic CO_2 enhancements were 36.20 ppm and 34.90 ppm. In comparison with the simulated biological CO_2 enhancements displayed in Figure 5a, both the observed and simulated CO_2 enhancements are indicative of a large anthropogenic (fossil fuel and cement production) CO_2 emission from the YRD.

Previous studies have also investigated urban CO_2 enhancements from a relatively broad range of developed environments worldwide. Verhulst et al. (2017) measured CO_2 mixing ratios at seven sites in Los Angeles, USA and concluded that the mean annual enhancement varied between 2.0 ppm and 30.8 ppm, which is considerably lower than our findings. Another study in Washington D.C., USA in February and July 2013 showed that the CO_2 enhancement was less than 20 ppm (Mueller et al., 2018). The urban CO_2 observations and modeling study by Martin et al. (2019) at three urban sites in eastern USA showed an enhancement of ~21 ppm in February 2013, substantially lower (by ~20 ppm) than our observations. The measurements at an urban-industrial complex site in Rotterdam, Netherlands, indicated a CO_2 enhancement of only 11 ppm for October to December 2014 (Super et al., 2017). Our enhancements were significantly higher than all of these previous reports of other urban areas.

The anthropogenic components and source area contributions are displayed in Figure 5b-c. During the study period the average anthropogenic enhancements were 5.1%, 80.2%, 1.9%, 4.4%, and 8.5% for Anhui, Jiangsu, Zhejiang, Shanghai, and the remaining area outside the YRD, respectively. Although Shanghai's area is the smallest within the YRD region and relatively distant (~300 km) from our observation site, its maximum source contribution at times exceeded 50% (i.e. on 19th September 2013, not shown) *via* long-distance transport. In general, power industry, manufacturing, non-metallic mineral production, oil refinery, and other source categories contributed 41.0%, 21.9%, 9.3%, 11.5%, and 16.3% to the total anthropogenic CO_2 enhancement, respectively. The proportions of corresponding CO_2 emission categories to the total anthropogenic emissions of the YRD were 39.8%, 28.4%, 7.4%, 4.1%, and 24.4%, respectively. The comparisons between the proportions of simulated enhancement and proportions of corresponding CO_2 emissions can illustrate whether CO_2 enhancement partitions is a good tracer for emissions in complex urban area. We found a relatively large difference between the enhancement proportion and the emission proportion for oil refineries (from 11.5% to 4.1%) as compared to other categories. This may be because power industry, manufacturing and non-metallic mineral production were more homogeneously distributed compared to oil refineries, which were closer to our CO_2 observation site. Further, changes in source footprint caused by wind direction variations likely played an important role.

3.1.3 Constraints on monthly anthropogenic CO_2 emissions

To provide a robust comparison of bottom-up CO_2 emissions for YRD, we calculated anthropogenic CO_2 emissions from both EDGAR v4.3.2 and with activity data provided by local governments (Table 1) and the default IPCC emission factors (https://www.ipcc-nggip.iges.or.jp/EFDB/). The total anthropogenic CO_2 emissions in 2014-2015 were 24.4×10^{11} kg and 23.5×10^{11} kg according to our own inventory and EDGAR v4.3.2 CO_2, respectively, indicating excellent agreement (within 4%) between these approaches. We constrained the monthly anthropogenic CO_2 emissions by using the MSF method (equation 8) and computed the 12-month average to represent the years of 2014 and 2015. The *a posteriori* results indicate that the annual scaling factors were 1.03 ± 0.10 for 2014 and 1.06 ± 0.09 for 2015. The monthly scaling factors derived from using daytime and all-day observations are also shown in Figure S4. These factors vary seasonally with higher values observed in summer. When using daytime values only, the scaling factors were much larger than the all-day values. This can be seen in Figure 3 by comparing the simulated and observed CO_2 mixing ratios. We should note here that the larger scaling factors based on the daytime data could be caused by bias in the *a priori* daily scaling factors used to generate the hourly CO_2 emissions (Hu et al., 2018b); the monthly anthropogenic averages; and bias in negative biological CO_2 enhancement. Since our study is mainly focused on the seasonality of all-day observations, the monthly scaling factors derived from the all-day approach will be used for the following analyses. The anthropogenic CO_2 emissions in year 2015 did not show a significant change compared to 2014, and the overall estimates were within the uncertainty of the estimates. After applying the average scaling factors for 2014 and 2015, the *a posteriori* anthropogenic CO_2 emissions were 24.6 (± 2.4) $\times 10^{11}$ kg for the YRD area. The application of the MSF method provides an overall constraint on the anthropogenic CO_2 emissions (also displayed in Table 1).

The main uncertainties associated with the simulation of hourly CO_2 and $\boldsymbol{\delta}^{13}C\text{-}CO_2$ are uncertainty in meteorological fields, transport model (i.e. number of released particles), and *a priori* CO_2 fluxes. At the annual scale the main uncertainty is attributed to the PBLH simulations and *a priori* anthropogenic CO_2 emissions. The anthropogenic CO_2 emissions biases were < 6% as described above, and the bias associated with PBLH uncertainty was typically <13% (Hu et al., 2018a; 2018b). There, we attribute a 20% uncertainty to the simulated CO_2 and $\boldsymbol{\delta}^{13}C\text{-}CO_2$ signals on an annual time scale.

3.2 Simulation of atmospheric $\boldsymbol{\delta}^{13}C\text{-}CO_2$

3.2.1 Background atmospheric δ^{13}C-CO$_2$

To obtain the best representative δ^{13}C-CO$_2$ background value for the study domain we examined the values from the three strategies described above (Figure 6). We also compared the δ^{13}C-CO$_2$ at the WLG background site with observations at NUIST during winters (Figure S5). This was performed to help simplify the comparison by removing the effects of plant photosynthetic discrimination. The δ^{13}C-CO$_2$ at the WLG site was relatively more depleted in the heavy carbon isotope (or negative, by up to 0.5‰) than that observed at NUIST for many periods. Theoretically, there are two key factors that can cause the urban atmospheric δ^{13}C-CO$_2$ to be relatively more enriched in the heavy carbon isotope (or positive) compared to the background values including: 1) Discrimination associated with ecosystem photosynthesis; and 2) Enrichment of isotopic signature associated with the CO$_2$ derived from cement production. As shown earlier, the biological CO$_2$ enhancement was positive in winter, which implies a positive biological CO$_2$ signal where ecosystem respiration is more important than photosynthesis. Further, sensitivity tests for cement CO$_2$ sources showed its influence is much smaller than the observed difference in Figure S5 (discussed in section 3.3.3). Based on the above analyses and methods introduced in Section 2.3, we concluded that the WLG δ^{13}C-CO$_2$ signal is not an ideal choice for representing the background value. The wintertime δ^{13}C-CO$_2$ background values, based on strategy 2, were -7.78‰ and -7.61‰ for 2013-2014 and 2014-2015, respectively (Figure 6). The corresponding values, based on strategy 3, were -7.70‰ and -7.53‰. These background values are more enriched compared to the WLG observations by 0.80‰ to 1.01‰. These derived values agree well with the monthly δ^{13}C-CO$_2$ simulation results of Chen et al. (2006) who showed that δ^{13}C-CO$_2$ is 0.6‰ higher above the PBL than in the surface layer near the ground. Recently, Ghasemifard et al. (2019) showed that hourly δ^{13}C-CO$_2$ values at Mount Zugspitze, the highest (2650 m) mountain in Germany, varied between -7‰ and -12‰ in the winter for 2013. During two especially clean air events (in October and February) at Mount Zugspitze, the δ^{13}C-CO$_2$ was approximately -7‰, during which the CO$_2$ mixing ratios varied between 390 and 395 ppm. This is consistent with our estimates using strategies 2 and 3. Based on the evidence presented above, we believe that strategy 3 is the most robust way to derive a background δ^{13}C-CO$_2$ for the study domain.

3.2.2 Evaluation of δ^{13}C-CO$_2$ simulations

Figure 7a shows the hourly δ^{13}C-CO$_2$ simulations over a two-year period. To the best of our knowledge, this is the first time that δ^{13}C-CO$_2$ has been simulated at an hourly time scale for an urban region. The simulations are consistent with the observations at daily, monthly and annual time scales, where the average value of observations (simulations) were -8.69‰ (-8.68‰) and -8.52‰ (-8.45‰) for 2014 and 2015, respectively. The corresponding correlation was R = 0.54 ($P < 0.001$) and R = 0.52 ($P < 0.001$).

The root mean square error between observations and simulations was 1.07‰ for 2014 and 1.10‰ for 2015 (Table 2). Further, the observed and simulated δ^{13}C-CO$_2$ values showed seasonal variations that increased in summer and decreased in winter. This pattern mirrored the CO$_2$ mixing ratios for both observations and simulations (Figures 3a and 8). Similar relations and seasonal variations of δ^{13}C-CO$_2$ have been reported in other urban areas (Sturm et al., 2006; Guha & Ghosh, 2010; Moore & Jacobson, 2015; Pang et al., 2016). The simulated hourly NEE CO$_2$ enhancement is also shown in Figure 7b. Note that negative values indicate net CO$_2$ sinks and positive values indicate net CO$_2$ sources. We can see large hourly variations in the growing seasons and positive enhancements during nighttime that are generally larger than negative enhancements during daytime. This shows the potential influence of NEE on δ^{13}C-CO$_2$ seasonality. To date, no study has quantified the relative contributions to the δ^{13}C-CO$_2$ seasonality. Here, we re-evaluate and quantify the main factors contributing to its seasonality based on the combination of δ^{13}C-CO$_2$ observations and simulations in the following section.

Here, we examine the comparisons for winter and summer in greater detail. The simulations showed that the model can generally capture the diel variations of observed hourly δ^{13}C-CO$_2$ variations (Figure 8). Statistics between observations and simulations for two seasons are shown in Table 2. The observed seasonal average increased substantially, by 1.18‰, from winter 2013-2014 (-9.27‰) to summer 2014 (-8.09‰). The simulations showed a similar seasonal increase of 1.35‰. Some large discrepancies are evident and generally caused by the simulated total CO$_2$ enhancement biases (potentially caused by poorly simulated PBLH during these periods) and the negative relationship between δ^{13}C-CO$_2$ and the CO$_2$ enhancement as shown in Figure S6.

Comparisons between observations and simulations for daily average CO$_2$ mixing ratio and δ^{13}C-CO$_2$ are also shown in Figure 9. Although the data are distributed around the 1:1 line for both seasons, there is less scatter and higher correlation in the winter than in the summer. We attributed this to the more complex biological CO$_2$ sinks in the summer, which are not adequately resolved by the relatively coarse model grid (1° by 1°). We also performed comparisons by only choosing the daytime observations. The results indicated that daytime CO$_2$ mixing ratio simulations in the summer were slightly underestimated. This caused δ^{13}C-CO$_2$ to be overestimated (Figure S7). The simulations for winter generally captured the trends for both CO$_2$ and δ^{13}C-CO$_2$ when the biological CO$_2$ enhancement played a relatively small role compared to anthropogenic emissions. The larger bias in the summer could result from the relatively coarse spatial-temporal resolution (aggregation error) of the Carbon Tracker biological CO$_2$ flux, which was 1×1 degree with three-hour average. As shown in Figure S3, the spatial distribution of land use is far more heterogeneous. This will smooth the stronger biological CO$_2$ signals by averaging it over the large

1×1 degree grid, while the urban biological CO_2 flux occurs at much finer spatial scales and likely varies at shorter time intervals.

3.2.3 Mechanisms controlling the $\boldsymbol{\delta}^{13}$C-CO_2 seasonality

The mechanisms driving these seasonal variations are examined below. The peak and trough in the observed $\boldsymbol{\delta}^{13}$C-CO_2 signal was observed in December and July (Figure 10a), respectively, yielding an amplitude of 1.51‰. This was consistent with the simulated amplitude of 1.53‰. These results support that the simulated $\boldsymbol{\delta}^{13}$C-CO_2 seasonality agreed well with the observations (Figure 10), and can be used to further diagnose the mechanisms contributing to the $\boldsymbol{\delta}^{13}$C-CO_2 seasonality. According to equation 2, the $\boldsymbol{\delta}^{13}$C-CO_2 seasonality can be attributed to four factors including: (1) A change in the background $\boldsymbol{\delta}^{13}$C-CO_2 value from -7.64‰ in December to -6.66‰ in July; (2) A change in CO_2 background from 399 ppm to 398 ppm; (3) The total CO_2 enhancement change from 45.7 ppm to 37.3 ppm; and (4) The change in the isotope composition of the CO_2 enhancements causing $\boldsymbol{\delta}$s to vary from -26.1‰ to -22.8‰.

To quantify each mechanism's contribution to the seasonality of atmospheric $\boldsymbol{\delta}^{13}$C-CO_2, we recalculated $\boldsymbol{\delta}^{13}$C-CO_2 by using the monthly averages as described above. First, we calculated $\boldsymbol{\delta}^{13}$C-CO_2 in December and July, which were -9.54‰ and -8.04‰, respectively, with amplitude of 1.50‰. Next, we replaced the $\boldsymbol{\delta}^{13}$C-CO_2 background value in December (-7.64‰) with July (-6.67‰). The recalculated $\boldsymbol{\delta}^{13}$C-CO_2 was -8.66‰ in December, indicating that the change in $\boldsymbol{\delta}^{13}$C-CO_2 background value caused a change of 0.88‰ (9.54‰ minus -8.66‰) to the seasonality. By changing both the total CO_2 enhancement and background values, the recalculated $\boldsymbol{\delta}^{13}$C-CO_2 was -8.32‰, contributing a 0.34‰ change in the seasonality (-8.66‰ minus -8.32‰). Finally, by changing $\boldsymbol{\delta}$s from -26.1‰ to -22.8‰, together with the change in background value, the recalculated $\boldsymbol{\delta}^{13}$C-CO_2 was -8.32‰ a change of 0.34‰ (i.e. -8.66‰ minus -8.32‰). This indicates that both the total CO_2 enhancement and change in $\boldsymbol{\delta}$s contributed equally to the regional source term, causing a variation of 0.62‰ (i.e. 1.50‰ minus 0.88‰). Based on the above analyses, we attributed 59% and 41% of the $\boldsymbol{\delta}^{13}$C-CO_2 seasonality to the changing $\boldsymbol{\delta}^{13}$C background term and regional source terms, respectively. Further, the total CO_2 enhancement and change in $\boldsymbol{\delta}$s, sum of both can be treated as regional source term, contributed equally (about 20%) to the $\boldsymbol{\delta}^{13}$C-CO_2 seasonality.

To investigate how ecosystem photosynthetic discrimination and respiration affected atmospheric $\boldsymbol{\delta}^{13}$C-CO_2 seasonality, we simulated the $\boldsymbol{\delta}^{13}$C-CO_2 again for two cases: (1) excluding negative NEE when photosynthesis is stronger than respiration, and (2) excluding both photosynthetic discrimination and respiration. Note that only NEE was used in our study with no partitioning between photosynthesis and respiration in the daytime. The only role of photosynthetic discrimination should be stronger than in case 1 when only negative NEE is used. The results are shown in Figure 10 b-c. Overall, the negative CO_2

enhancement caused atmospheric $\boldsymbol{\delta}^{13}$C-CO$_2$ to become more enriched in the baseline simulations with maximum values around 1‰ between April and October (Figure 10b), and positive CO$_2$ enhancement (i.e. via net respiration) caused atmospheric $\boldsymbol{\delta}^{13}$C-CO$_2$ to become more depleted compared to the baseline simulations through the whole year (Figure 10c). By applying the CCGRCV fitting technique to the $\boldsymbol{\delta}^{13}$C-CO$_2$ for the above two cases, we found that the $\boldsymbol{\delta}^{13}$C-CO$_2$ seasonality decreased to 1.45‰ in case 1, indicating ecosystem photosynthetic discrimination explained > 0.08‰ of the seasonality (1.53‰ minus 1.45‰). For case 2, the $\boldsymbol{\delta}^{13}$C-CO$_2$ trough in winter slightly increased by 0.08‰ and peak in summer increased by 0.20‰, these two factors finally lead the seasonality increase to 1.66‰, which were caused by much larger respiration CO$_2$ enhancement in summer than in winter (Figure 7b). These results indicate that biological respiration reduced the $\boldsymbol{\delta}^{13}$C-CO$_2$ seasonality by 0.20‰, and that negative NEE (photosynthetic discrimination) acted to increase the $\boldsymbol{\delta}^{13}$C-CO$_2$ seasonality by 0.08‰. Generally, both ecosystem photosynthesis and respiration played minor roles in controlling the atmospheric $\boldsymbol{\delta}^{13}$C-CO$_2$ seasonality within this urban area. In other words, the anthropogenic CO$_2$ emissions played a much larger role than the plants.

As shown in Figure 5, CO$_2$ sources from power industry, combustion for manufacturing, non-metallic mineral production and oil refineries and transformation industry were the top 4 contributors to the CO$_2$ enhancements. We simulated atmospheric $\boldsymbol{\delta}^{13}$C-CO$_2$ by assuming that no CO$_2$ was emitted from each of these 4 categories. The simulations were performed by excluding one category at a time. The results indicated that atmospheric $\boldsymbol{\delta}^{13}$C-CO$_2$ seasonality was 1.30‰, 1.57‰, 1.30‰, and 1.47‰, if excluding power industry, combustion for manufacturing source, oil refineries/transformation industry, and non-metallic mineral production sources, respectively. In other words, power industry and oil refineries/ transformation industry together contributed 0.40‰ to the total regional source term of 0.62‰. The cement sources played a role in enriching 0.07‰ the atmospheric $\boldsymbol{\delta}^{13}$C-CO$_2$ in the heavy isotope, contrary to all other anthropogenic CO$_2$ sources.

3.3 Sensitivity analysis

3.3.1 Comparison of $\boldsymbol{\delta}$s·$\boldsymbol{\Delta}$CO$_2$

Based on equation 2, the regional source term determines the hourly/daily variations of $\boldsymbol{\delta}^{13}$C-CO$_2$, which is treated as a signal added to the background signal. To evaluate the model simulated regional source term with respect to the observations we examined daily averages for winter to minimize the influence of photosynthesis. In Figure 11a, the observed daily $\boldsymbol{\delta}$s·$\boldsymbol{\Delta}$CO$_2$ values are compared with the simulated values using the *a priori* anthropogenic CO$_2$ emissions. Here $\boldsymbol{\Delta}$CO$_2$ represents the total CO$_2$ enhancement for both observations and simulations. The product $\boldsymbol{\delta}$s·$\boldsymbol{\Delta}$CO$_2$ can be interpreted as the regional source term.

The average values were -1009.0 (and -841.9) ppm·‰ for observations and -1096.7 (and 1000.5) ppm·‰ for model results in 2014 (and 2015). The slope of the regression fit was 0.99 (±0.12) and the intercept was -151.7 (±130.1) for all data during the two winters. After applying the monthly scaling factors to constrain the anthropogenic CO_2 emissions, the re-calculated results were closer to the 1:1 line with a slightly improved correlation (R increased from 0.47 to 0.50; Figure 11b). Note that the application of the monthly scaling factors only impacts the ΔCO_2 but not δs. The uncertainty in δs will be discussed next.

3.3.2 Comparison between δ_{s_sim} and δ_s

To evaluate the δ_s simulations, we compared observed and simulated δ_s as displayed in Figure 12a for all-day and nighttime conditions. Here, nighttime simulations were selected to minimize the effects of ecosystem photosynthesis and to mainly focus on the anthropogenic CO_2 sources. Two methods were used to calculate δ_s from the observations including the Miller-Tans and Keeling plot methods. Although δ_s differed between these two methods, both displayed similar seasonal variations with higher values ($\delta^{13}C$ enrichment) in summer and lower values in winter. Such seasonal variations were also observed at other urban sites including Beijing, China (Pang et al., 2016), Bern, Switzerland (Sturm et al., 2006), Bangalore city, India (Guha and Ghosh, 2010),Wroclaw, Poland (Górka and Lewicka-szczebak, 2013).

If the CO_2 sources/sinks are homogeneously distributed and without monthly variations, the atmospheric CO_2 enhancement components would remain unchanged, and there would be no seasonal changes in δ_s. In reality, variations in atmospheric transport processes interact with regional CO_2 sink/source changes that cause monthly variations in δ_s. The comparison of δ_s between simulations and observations indicated that the model performed well in capturing the mixing and transport of CO_2 from different sources. We can also infer from their difference that the proportions of some CO_2 categories were biased in the *a priori* emission map. This can be caused by both the downscaling of EDGAR inventory distribution to 0.1° and the magnitude of some emissions categories. Among all anthropogenic sources, the most significant linear relations were found between the simulated anthropogenic δ_s and cement CO_2 proportions for these 24 months, with slopes of 0.33‰ for nighttime and 0.35‰ for all-day conditions ($R^2 = 0.97$, $p < 0.001$; Figure 12 b & c). These results also indicated that cement CO_2 emissions dominated monthly δs variations in the YRD region.

3.3.3 Sensitivity of atmospheric $\delta^{13}C$-CO_2 and δ_s to cement CO_2 emissions

The discrepancy between simulated and observed δ_s highlights that some CO_2 sources were biased in the *a priori* inventories. As discussed above, cement CO_2 emissions had the most distinct $\delta^{13}C$-CO_2 end-member value of 0‰ ± 0.30‰ when compared with the averages of other anthropogenic sources.

Combined with its large emission compared to other regions of the world, it had a strong potential to influence $\boldsymbol{\delta}_{\mathrm{s}}$ and $\boldsymbol{\delta}^{13}$C-CO$_2$. YRD represents the largest cement producing region in the world (USGS, 2014; Cai et al., 2015; Yang et al., 2017). Its relative proportion to total national anthropogenic CO$_2$ emissions is about 5.5% to 6.5% based on IPCC method and 7.3% for EDGAR. These proportions are 50% greater than the global average of 4% (Boden et al., 2016) and much larger than most countries (Andrew, 2018) and other large urbanized areas such as California (2%; Cui et al., 2019).

The local activity data reveals that the cement production increased from 3.55×10^{8} tons in 2010 to 4.56×10^{8} tons in 2014 in the YRD area. Our own calculation of the national clinker-to-cement indicated a decreasing trend from 64% in 2004 to around 56% in 2015. Here, we applied the value of 61.7% for 2010 and the average value of 57.0% for 2014 to 2015. We then used the EF for clinker (0.52 ± 0.01 tonne CO$_2$ per tonne clinker; IPCC 2013). Finally, the calculated cement CO$_2$ emissions were $1.14\ (\pm\ 0.02) \times 10^{8}$ tonne for 2010 and $1.35\ (\pm 0.03) \times 10^{8}$ tonne for 2014, indicating an 18.4% increase over this time period. This result is close to the scaling factor 1.145 for the total anthropogenic CO$_2$ emissions for the same period.

The cement CO$_2$ emission was 1.45×10^{8} tonne for the EDGAR products in 2010. Applying the scaling factor of 1.184, based on our independent method, the EDGAR cement CO$_2$ emissions was 1.72×10^{8} tonne for the year of 2014. The 27% difference between the EDGAR inventory and our independent calculations probably resulted from large errors in the clinker-to-cement ratio and regional activity data. Ke et al. (2013) reported a much higher clinker-to-cement ratio of 73% to 70% for China during 2005 and 2007 than the ratio of 57% in 2014 to 2015. If we applied a 70% ratio, the EDGAR cement CO$_2$ emission would change to 1.28×10^{8} tonne for 2010.

The monthly cement emission proportions varied from 6.21% to 8.98%, while its enhancement proportion was much larger and could reach 16.85%. In other words, favorable atmospheric transport processes amplified the cement CO$_2$ enhancement proportion at our observational site (Table S2). To quantify the extent to which the cement CO$_2$ enhancement components can affect $\boldsymbol{\delta}$s and atmospheric $\boldsymbol{\delta}^{13}$C-CO$_2$ we conducted sensitivity tests by changing the cement enhancement proportions to 0.8, 1.2, 1.4, 1.6, 1.8, and 2 times its original value. These sensitivity tests are based on two different assumptions for cement CO$_2$ enhancement changes: (1) There is no bias in the total anthropogenic CO$_2$ enhancement such that a proportional increase/decrease in the cement component does not change the relative anthropogenic contributions; (2) Only the cement enhancement changes. From equation 2, these two assumptions will change both $\boldsymbol{\delta}$s and $\boldsymbol{\delta}^{13}$C-CO$_2$ but with different amplitude.

Results for the first assumption are shown in Figure 13a-b for both nighttime and all-day $\boldsymbol{\delta}_s$ simulations. The simulated $\boldsymbol{\delta}_s$ increased linearly with the increase of cement proportions, at a rate of 2.73‰ increase per 10% increase of cement proportions in the nighttime and 2.72‰ for all-day. The result for the second assumption is similar to the first one, yielding a 2.32‰ increase for a 10% increase in the cement proportion. As shown in Table S2, the cement CO_2 enhancement proportions increased from 5.60% - 6.77% (December) to 13.16% - 16.85% (June), which is the primary cause for the observed monthly $\boldsymbol{\delta}_s$ variations. The high sensitivity of $\boldsymbol{\delta}_s$ to cement CO_2 proportions can partly explain the relative difference of modeled $\boldsymbol{\delta}_s$ and indicates a potential advantage to constrain cement CO_2 emissions by using atmospheric $\boldsymbol{\delta}^{13}$C-CO_2 observations. Finally we calculated how cement CO_2 can change atmospheric $\boldsymbol{\delta}^{13}$C-CO_2 (Figure 13c). These results show that atmospheric $\boldsymbol{\delta}^{13}$C-CO_2 is more sensitive to the first assumption than the second assumption. These sensitivity analyses indicate that a cement CO_2 enhancement relative change of 20% (or absolute 1.57% increase) can cause a 0.013‰ - 0.038‰ change in the atmospheric $\boldsymbol{\delta}^{13}$C-CO_2. These results indicate that $\boldsymbol{\delta}_s$ is sensitive to cement CO_2 emissions.

4 Conclusions

(1) Total annual anthropogenic CO_2 emissions for the YRD showed high consistency between the top-down and bottom-up approaches with a bias less than 6%.

(2) Approximately 59% and 41% of the $\boldsymbol{\delta}^{13}$C-CO_2 seasonality was attributed to the change in $\boldsymbol{\delta}^{13}$C background value and the regional CO_2 source term, respectively.

(3) Power industry and oil refineries/ transformation industry together contributed 0.40‰ to the seasonal cycle, accounting for 64.5% in all regional source terms (0.62‰).

(4) If excluding all ecosystem respiration and photosynthetic discrimination in YRD area, $\boldsymbol{\delta}^{13}$C-CO_2 seasonality will increase from 1.53‰ to 1.66‰.

(5) Atmospheric transport processes in summer amplified the cement CO_2 enhancement proportions in the YRD area, which dominated monthly $\boldsymbol{\delta}$s variations. $\boldsymbol{\delta}_s$ calculated from simulations was shown to be a strong linear relation with cement CO_2 EDGAR v4.3.2 inventory proportion in the YRD area.

Acknowledgements

This work is supported by the National Key R&D Program of China (grants 2020YFA0607501 & 2019YFA0607202 to Xiao Wei), Cheng Hu acknowledges support from the Natural Science Foundation of Jiangsu Province (BK20200802), this work is also supported by National Natural Science Foundation of China (grant no.42021004), Natural Science Foundation of Jiangsu Province (BK20181100), and Key Research Foundation of Jiangsu Meteorological Society (KZ201803).

Code/Data availability

The data presented in this manuscript has been uploaded on our group website: https://yncenter.sites.yale.edu/data-access.

Author contribution: Cheng Hu, Timothy J. Griffis and Xuhui Lee designed the study, Cheng Hu performed the model simulation and wrote the original draft, Supervision: Timothy J. Griffis and Xuhui Lee, Data acquisition: Jiaping Xu, Wenjing Huang, Dong Yang, Yan Chen, Cheng Liu, Shoudong Liu, and Lichen Deng, all co-authors contributed to the data analysis.

Competing interests: The authors declare that they have no conflict of interest.

References:

Alden, C. B., Miller, J. B., and Gatti, L. V.: Regional atmospheric CO_2 inversion reveals seasonal and geographic differences in Amazon net biome exchange, *Global Change Biology*, 22, 3427–3443, https://doi.org/10.1111/gcb.13305, 2016.

Andrew, R. M.: Global CO_2 emissions from cement production, *Earth System Science Data*, 10, 2213–2239. https://doi.org/10.5194/essd-2017-77, 2018.

Ballantyne, A. P., Miller, J. B., Baker, I. T., Tans, P. P., and White, J. W. C.: Novel applications of carbon isotopes in atmospheric CO_2: what can atmospheric measurements teach us about processes in the biosphere? *Biogeosciences*, 8, 3093– 3106, https://doi.org/10.5194/bg-8-3093-2011, 2011.

Boden, T., Andres, R., and Marland, G.: Global, Regional, and National Fossil-Fuel CO_2 Emissions (1751 - 2013) (V. 2016) [Data set]. Environmental System Science Data Infrastructure for a Virtual Ecosystem; Carbon Dioxide Information Analysis Center (CDIAC), Oak Ridge National Laboratory (ORNL), Oak Ridge, TN (United States).

Berezin, E. V., Konovalov, I. B., Ciais, P., Richter, A., Tao, S., Janssens-Maenhout, G., Beekmann, M., and Schulze, E.-D.: Multiannual changes of CO_2 emissions in China: indirect estimates derived from satellite measurements of tropospheric NO_2 columns, Atmos. Chem. Phys., 13, 9415–9438, https://doi.org/10.5194/acp-13-9415-2013, 2013.

Brioude, J., Angevine, W. M., Ahmadov, R., Kim, S.-W., Evan, S., McKeen, S. A., Hsie, E.-Y., Frost, G. J., Neuman, J. A., Pollack, I. B., Peischl, J., Ryerson, T. B., Holloway, J., Brown, S. S., Nowak, J. B., Roberts, J. M., Wofsy, S. C., Santoni, G. W., Oda, T., and Trainer, M.: Top-down estimate of surface flux in the Los Angeles Basin using a mesoscale inverse modeling technique: assessing anthropogenic emissions of CO, NO_x and CO_2 and their impacts, Atmos. Chem. Phys., 13, 3661–3677, https://doi.org/10.5194/acp-13-3661-2013, 2013.

Bréon, F. M., Broquet, G., Puygrenier, V., Chevallier, F., Xueref-Remy, I., Ramonet, M., Dieudonné, E., Lopez, M., Schmidt, M., Perrussel, O., and Ciais, P.: An attempt at estimating Paris area CO_2 emissions from atmospheric concentration measurements, Atmos. Chem. Phys., 15, 1707–1724, https://doi.org/10.5194/acp-15-1707-2015, 2015.

Cao, C., Lee, X., Liu, S., Schultz, N., Xiao, W., Zhang, M., and Zhao, L.: Urban heat islands in China enhanced by haze pollution. *Nature Communications*, 7(1), doi: 10.1038/ncomms12509, 2016.

Chen, B., Chen J., Tans, P., and Huang L.: Simulating dynamics of $\delta^{13}C$ of CO_2 in the planetary boundary layer over a boreal forest region : covariation between surface fluxes and atmospheric mixing, *Tellus*, 537–549, https://doi.org/10.1111/j.1600-0889.2006.00213.x, 2006.

Chen, J. M., Mo, G., and Deng, F.: A joint global carbon inversion system using both CO2 and 13CO2 atmospheric concentration data, Geosci. Model Dev., 10, 1131–1156, https://doi.org/10.5194/gmd-10-1131-2017, 2017.

Cai B., Wang J., He J., and Geng Y.: Evaluating CO_2 emission performance in China's cement industry: An enterprise perspective. *Applied Energy*, 2015.11.006, https://doi.org/10.1016/j.apenergy.2015.11.006, 2015.

Cui, X., Newman, S., Xu, X., Andrews, A. E., Miller, J., Lehman, S.: Atmospheric observation-based estimation of fossil fuel CO_2 emissions from regions of central and southern California. *Science of the Total Environment*, 664, 381–391, https://doi.org/10.1016/j.scitotenv.2019.01.081, 2019.

Deng L., Liu S., and Zhao X., Study on the change in land cover of Yangtze River Delta based on MOD13A2 data, *China Science Paper*, 000(015):1822-1827 (in Chinese).

Gately, C. K., Hutyra, L. R., and Wing, I. S.: Cities, traffic, and CO_2 : A multidecadal assessment of trends, drivers , and scaling relationships, *Proceedings of the National Academy of Sciences of the United States of America*, 112(16), 4999–5004, https://doi.org/10.1073/pnas.1421723112, 2015.

Gately, C. K., and Hutyra, L. R.: Large uncertainties in urban-scale carbon emissions. *Journal of Geophysical Research: Atmospheres*, 122, 11,242–11,260, https://doi.org/10.1002/2017JD027359, 2017.

Ghasemifard, H., Vogel, F. R., Vardag, et al. Pollution Events at the High-Altitude Mountain Site Zugspitze-Schneefernerhaus (2670 m a.s.l.), Germany[J]. Atmosphere, 2019, 10(6).

Graven, H. D., Fischer, M. L., Lueker, T., Jeong, S., Guilderson, T. P., Keeling, R.: Assessing fossil fuel CO_2 emissions in California using atmospheric observations and models. *Environmental Research Letters*, 13(2018) 065007, https://doi.org/ 10.1088/1748-9326/aabd43, 2018.

Griffis, T. J., Sargent, S., Baker, J., Lee, X., Tanner, B., Greene, J., Swiatek, E., and K. Billmark K.: Direct measurement of biosphere-atmosphere isotopic CO_2 exchange using the eddy covariance technique, *Journal of Geophysical Research: Atmospheres*, 113, D08304, 2008.

Griffis, Timothy J.: Tracing the flow of carbon dioxide and water vapor between the biosphere and atmosphere : A review of optical isotope techniques and their application. *Agricultural and Forest Meteorology*, 174–175, 85–109, 2013.

Górka, M., and Lewicka-Szczebak, D.: One-year spatial and temporal monitoring of concentration and carbon isotopic composition of atmospheric CO_2 in a Wroclaw (SW Poland) city area. *Applied Geochemistry, 35:7-13,* https://doi.org/10.1016/j.apgeochem.2013.05.010, 2013.

Guha, T., and Ghosh, P.: Diurnal variation of atmospheric CO_2 concentration and δ^{13}C in an urban atmosphere during winter-role of the Nocturnal Boundary Layer. *Journal of Atmospheric Chemistry*, 65(1), 1–12, https://doi.org/ 10.1007/s10874-010-9178-6, 2010.

Hu, C., Liu, S., Wang, Y., Zhang, M., Xiao, W., Wang, W., and Xu, J.: Anthropogenic CO_2 emissions from a megacity in the Yangtze River Delta of China. *Environmental Science and Pollution Research*, 25(23), 23157–23169, https://doi.org/10.1007/s11356-018-2325-3, 2018a.

Hu, C., Griffis, T. J., Liu, S., Xiao, W., Hu, N., Huang, W., Yang D., and Lee X.: Anthropogenic methane emission and its partitioning for the Yangtze River Delta region of China. *Journal of Geophysical Research: Biogeosciences*, 124, https://doi.org/10.1029/2018JG004850, 2019.

Hu, C., Griffis, T. J., Lee, X., Millet, D. B., Chen, Z., Baker, J. M., and Xiao, K.: Top-Down constraints on anthropogenic CO_2 emissions within an agricultural-urban landscape. *Journal of Geophysical Research: Atmospheres*, 123(9), 4674–4694, https://doi.org/10.1029/2017JD027881, 2018b.

Hu, L., Andrews, A. E., Thoning, K. W., Sweeney, C., Miller, J. B., Michalak, A. M.: Enhanced North American carbon uptake associated with El Niño. *Science Advances*, 5, eaaw0076, https://doi.org/10.1126/sciadv.aaw0076, 2019.

He, J., Naik, V., Horowitz, L. W., Dlugokencky, E., and Thoning, K.: Investigation of the global methane budget over 1980–2017 using GFDL-AM4.1, Atmos. Chem. Phys., 20, 805–827, https://doi.org/10.5194/acp-20-805-2020, 2020.

IPCC (Intergovernmental Panel on Climate Change): 2019 Refinement to the 2006 IPCC Guidelines for National Greenhouse Gas Inventories, available at: https://www.ipcc-nggip.iges.or.jp/ public/2019rf/ (last access: 24 April 2021), 2019

IEA, 2012. CO_2 Emissions from Fuel Combustion 1971–2010, 2012 Edition. International Energy Agency (IEA), Paris 2012.

Janssens-Maenhout, G., Crippa, M., Guizzardi, D., Muntean, M., Schaaf, E., Dentener, F.: EDGAR v4.3.2 Global Atlas of the three major Greenhouse Gas Emissions for the period 1970-2012. Earth System Science Data Discussions, (August), 1–55. https://doi.org/10.5194/essd-2017-79, 2017.

Jiang, F., Wang, H. M., Chen, J. M., Machida, T., Zhou, L. X., Ju, W. M., Matsueda, H., and Sawa, Y.: Carbon balance of China constrained by CONTRAIL aircraft CO_2 measurements, Atmos. Chem. Phys., 14, 10133–10144, https://doi.org/10.5194/acp-14-10133-2014, 2014.

Ke J., Mcneil M., Price L., and Zhou N.: Estimation of CO_2 emissions from China's cement production: Methodologies and uncertainties[J]. *Energy Policy*, 57:172-181, https://doi.org/10.1016/j.enpol.2013.01.028, 2013.

Keeling, C. D.: The concentration and isotopic abundances of carbon dioxide in the atmosphere. Tellus, 12(2), 200–203. Keeling, C. D. (1961). The concentration and isotopic abundances of carbon dioxide in rural and marine air. *Geochimica et Cosmochimica Acta*, 24(3-4), 277–298, https://doi.org/10.1111/j.2153-3490.1960.tb01300.x, 1960.

Lai, C., Ehleringer, J. R., Tans, P., and Wofsy, S. C.: Estimating photosynthetic ^{13}C discrimination in terrestrial CO_2 exchange from canopy to regional scales, *Global Biogeochemical Cycles*, 18, GB1041, https://doi.org/1010.1029/2003gb002148, 2014.

Li, X., and Xiao, J.: A global, 0.05-degree product of solar-induced chlorophyll fluorescence derived from OCO-2, MODIS, and reanalysis data. *Remote Sensing*, 11, 517, https://doi.org/10.3390/rs11050517, 2019.

Lauvaux, T., Miles, N. L., Deng, A., Richardson, S. J., Cambaliza, M. O., Davis, K. J., and Wu K.: High-resolution atmospheric inversion of urban CO_2 emissions during the dormant season of the Indianapolis flux experiment (INFLUX). *Journal of Geophysical Research: Atmospheres*, 121(10), 5213–5236, https://doi.org/10.1002/2015JD024473, 2016.

Martin, C. R., Zeng, N., Karion, A., Mueller, K., Ghosh, S., Lopez-coto, I.: Investigating sources of variability and error in simulations of carbon dioxide in an urban region. *Atmospheric Environment*, 199, 55–69, https://doi.org/10.1016/j.atmosenv.2018.11.013, 2019.

Moore, J., & Jacobson, A. D. (2015). Seasonally varying contributions to urban CO_2 in the Chicago , Illinois , USA region : Insights from a high-resolution CO_2 concentration and $\delta^{13}C$ record, *Elementa: Science of the Anthropocene*, 3:000052.

Mueller, K., Yadav, V., Lopez-Coto, I., Karion, A., Gourdji, S., Martin, C., and Whetstone, J.: Siting Background Towers to Characterize Incoming Air for Urban Greenhouse Gas Estimation: A Case Study in the Washington, DC/Baltimore Area. *Journal of Geophysical Research: Atmospheres*, 123(5), 2910–2926, https://doi.org/10.1002/2017JD027364, 2018.

McManus, J.B., Nelson, D.D., Zahniser, M.S.: Long-term continuous sampling of $^{12}CO_2$, $^{13}CO_2$ and $^{12}C^{18}O^{16}O$ in ambient air with a quantum cascade laser spectrometer. *Isotopes in Environmental and Health Studies*, 46:1, 49-63, https://doi.org/10.1080/10256011003661326, 2010.

Miller, J. B., Tans, P. P., White, J. W. C., Conway, T. J., and Vaughn, B. W.: The atmospheric signal of terrestrial carbon isotopic discrimination and its implication for partitioning carbon fluxes, *Tellus B*, 55, 197–206, https://doi.org/10.1034/j.1600-0889.2003.00019.x, 2003.

Miller JB, Lehman SJ, Verhulst KR, Miller CE, Duren RM, Yadav V, Newman S, and Sloop CD. Large and seasonally varying biospheric CO2 fluxes in the Los Angeles megacity revealed by atmospheric radiocarbon. Proc Natl Acad Sci U S A, 2020; 117 (43) 26681-26687; doi.org/10.1073/pnas.2005253117.

Nathan, B., Lauvaux, T., Turnbull, J. C., and Richardson, S.: Source Sector Attribution of CO_2 Emissions Using an Urban CO/CO_2 Bayesian Inversion System. *Journal of Geophysical Research: Atmospheres*, 123, 13611-13621, https://doi.org/10.1029/2018JD029231, 2018.

Newman, S., Xu, X., Affek, H. P., Stolper, E., and Epstein S.: Changes in mixing ratio and isotopic composition of CO_2 in urban air from the Los Angeles basin, California, between 1972 and 2003, *Journal of Geophysical Research*, 113, D23304, https://doi.org/10.1029/2008JD009999, 2008.

Newman, S., Xu, X., Gurney, K. R., Hsu, Y. K., Li, K. F., Jiang, X., Keeling, R., Feng, S., O'Keefe, D., Patarasuk, R., Wong, K. W., Rao, P., Fischer, M. L., and Yung, Y. L.: Toward consistency between trends in bottom-up CO_2 emissions and top-down atmospheric measurements in the Los Angeles megacity, Atmos. Chem. Phys., 16, 3843–3863, https://doi.org/10.5194/acp-16-3843-2016, 2016.

Oda, T., Maksyutov, S., and Andres, R. J.: The Open-source Data Inventory for Anthropogenic CO_2, version 2016 (ODIAC2016): a global monthly fossil fuel CO_2 gridded emissions data product for tracer transport simulations and surface flux inversions, Earth Syst. Sci. Data, 10, 87–107, https://doi.org/10.5194/essd-10-87-2018, 2018.

Pang, J., Wen, X., and Sun, X.: Mixing ratio and carbon isotopic composition investigation of atmospheric CO_2 in Beijing, China. *Science of the Total Environment*, 539, 322–330, https://doi.org/10.1016/j.scitotenv.2015.08.130, 2016.

Peters, W., Jacobson, A. R., Sweeney, C., Andrews, A. E., Conway, T. J., Masarie, K., John B. M., Lori M. P. B., Gabrielle P., Adam I. H., Douglas E. J. W., Guido R. v., James T. R., Paul O. W., Maarten C. K., and Pieter P. T.: An atmospheric perspective on North American carbon dioxide exchange: CarbonTracker. *Proceedings of the National Academy of Sciences*, 104(48), 18925–18930, https://doi.org/10.1073/pnas.0708986104, 2007.

Pataki, D. E., Bowling, D. R., Ehleringer, J. R., and Zobitz, J. M.: High resolution atmospheric monitoring of urban carbon dioxide sources, *Geophysical Research Letter*, 33, L03813, https://doi.org/10.1029/2005GL024822, 2006.

Pillai, D., Buchwitz, M., Gerbig, C., Koch, T., Reuter, M., Bovensmann, H., Marshall, J., and Burrows, J. P.: Tracking city CO_2emissions from space using a high-resolution inverse modelling approach: a case study for Berlin, Germany, Atmos. Chem. Phys., 16, 9591–9610, https://doi.org/10.5194/acp-16-9591-2016, 2016.

Prairie, Y. T. and Duarte, C. M.: Direct and indirect metabolic CO2 release by humanity, Biogeosciences, 4, 215–217, doi:10.5194/bg-4-215-2007, 2007.

Ruckstuhl, A. F., Henne, S., Reimann, S., Steinbacher, M., Vollmer, M. K., O'Doherty, S., Buchmann, B., and Hueglin, C.: Robust extraction of baseline signal of atmospheric trace species using local regression, Atmos. Meas. Tech., 5, 2613–2624, https://doi.org/10.5194/amt-5-2613-2012, 2012.

Rayner, P. J., Raupach, M. R., Paget, M., Peylin, P., and Koffi, E.: A new global gridded data set of CO2 emissions from fossil fuel combustion : Methodology and evaluation, Journal of Geophysical Research: Atmospheres. 115, D19306, https://doi.org/10.1029/2009JD013439, 2010.

Ribeiro, H. V, Rybski, D., and Kropp, J. P.: Effects of changing population or density on urban carbon dioxide emissions. Nature Communications, (2019), 1–9, https://doi.org/10.1038/s41467-019-11184-y, 2019.

Sargent, M., Barrera, Y., Nehrkorn, T., Hutyra, L. R., Gately, C. K., Mckain, K., Sweeney, C., Hegarty, J., Hardiman, B., Steven C. Wofsy, S. C.: Anthropogenic and biogenic CO_2 fluxes in the Boston urban region, Proceedings of the National Academy of Sciences of the United States of America. 115(40), https://doi.org/10.1073/pnas.1803715115, 2018.

Schneising, O., Heymann, J., Buchwitz, M., Reuter, M., Bovensmann, H., and Burrows, J. P.: Anthropogenic carbon dioxide source areas observed from space: assessment of regional enhancements and trends, Atmos. Chem. Phys., 13, 2445–2454, https://doi.org/10.5194/acp-13-2445-2013, 2013.

Staufer, J., Broquet, G., Bréon, F.-M., Puygrenier, V., Chevallier, F., Xueref-Rémy, I., Dieudonné, E., Lopez, M., Schmidt, M., Ramonet, M., Perrussel, O., Lac, C., Wu, L., and Ciais, P.: The first 1-year-long estimate of the Paris region fossil fuel CO2 emissions based on atmospheric inversion, Atmos. Chem. Phys., 16, 14703–14726, https://doi.org/10.5194/acp-16-14703-2016, 2016.

Sturm, P., Leuenberger, M., Valentino, F. L., Lehmann, B., and Ihly, B.: Measurements of CO2, its stable isotopes, O2/N2, and 222Rn at Bern, Switzerland, Atmos. Chem. Phys., 6, 1991–2004, https://doi.org/10.5194/acp-6-1991-2006, 2006.

Sturm, P., Tuzson, B., Henne, S., and Emmenegger, L.: Tracking isotopic signatures of CO2 at the high altitude site Jungfraujoch with laser spectroscopy: analytical improvements and representative results, Atmos. Meas. Tech., 6, 1659–1671, https://doi.org/10.5194/amt-6-1659-2013, 2013.

Super, I., Denier van der Gon, H. A. C., van der Molen, M. K., Sterk, H. A. M., Hensen, A., and Peters, W.: A multi-model approach to monitor emissions of CO2 and CO from an urban–industrial complex, Atmos. Chem. Phys., 17, 13297–13316, https://doi.org/10.5194/acp-17-13297-2017, 2017.

State Statistical Bureau. China Statistical Yearbook 2015; China Statistical Press: Beijing, China, 2016. (In Chinese)

Seto, K. C., Dhakal, S., Bigio, A., Blanco, H., Delgado, G. C., and Dewar, D.: Human settlements, infrastructure, and spatial planning. In O. Edenhofer, et al. (Eds.), Climate change 2014: Mitigation ofclimate change. Contribution ofworking group III to the fifth assessment report of the intergovernmental panel on climate change (pp. 923–1000). Cambridge, UK and New York, NY, USA: Cambridge University Press. https://doi.org/10.1017/CBO9781107415416.018, 2014.

Thompson, R. L., Patra, P. K., Chevallier, F., Maksyutov, S., Law, R. M., Ziehn, T., and Ciais P.: Top-down assessment of the Asian carbon budget since the mid 1990s. Nature Communications, 7, 1–10, https://doi.org/10.1038/ncomms10724, 2016.

Turnbull, J. C., Sweeney, C., Karion, A., Newberger., T., Lehman, S. J., Tans P. P., Davis, K.: Toward quantification and source sector identification of fossil fuel CO2 emissions from an urban area: results from the influx experiment. Journal of Geophysical Research: Atmospheres, 120(1, 292):–312, https://doi.org/10.1002/2014JD022555, 2015.

Turner, A. J., Shusterman, A. A., McDonald, B. C., Teige, V., Harley, R. A., and Cohen, R. C.: Network design for quantifying urban CO2 emissions: assessing trade-offs between precision and network density, Atmos. Chem. Phys., 16, 13465–13475, https://doi.org/10.5194/acp-16-13465-2016, 2016.

Thoning, K. W., Tans, P. P., and Komhyr, W. D.: Atmospheric carbon dioxide at Mauna Loa observatory 2. Analysis of the NOAA/GMCC data, 1974–1985. *Journal of Geophysical Research: Atmospheres*, 94(D6), 8549–8565, https://doi.org/10.1029/JD094iD06p08549 ,1989.

USGS (U. S. Geological Survey), 2014. Mineral Commodity Summaries 2013.http://minerals.usgs.gov/

minerals/pubs/commodity/cement/.

Wang, Y., Munger, J. W., Xu, S., McElroy, M. B., Hao, J., Nielsen, C. P., and Ma, H.: CO_2 and its correlation with CO at a rural site near Beijing: implications for combustion efficiency in China, Atmos. Chem. Phys., 10, 8881–8897, https://doi.org/10.5194/acp-10-8881-2010, 2010.

Zhang, H. F., Chen, B. Z., van der Laan-Luijkx, I. T., Chen, J., Xu, G., Yan, J. W., Zhou, L. X., Fukuyama, Y., Tans, P. P., and Peters W.: Net terrestrial CO_2 exchange over China during 2001–2010 estimated with an ensemble data assimilation system for atmospheric CO_2, *Journal of Geophysical Research: Atmospheres*, 119, 3500–3515, https://doi.org/10.1002/2013JD021297, 2014.

Vardag, S. N., Gerbig, C., Janssens-Maenhout, G., and Levin, I.: Estimation of continuous anthropogenic CO_2: model-based evaluation of CO_2, CO, $\delta^{13}C(CO_2)$ and $\Delta^{14}C(CO_2)$ tracer methods, Atmos. Chem. Phys., 15, 12705–12729, https://doi.org/10.5194/acp-15-12705-2015, 2015.

Verhulst, K. R., Karion, A., Kim, J., Salameh, P. K., Keeling, R. F., Newman, S., Miller, J., Sloop, C., Pongetti, T., Rao, P., Wong, C., Hopkins, F. M., Yadav, V., Weiss, R. F., Duren, R. M., and Miller, C. E.: Carbon dioxide and methane measurements from the Los Angeles Megacity Carbon Project – Part 1: calibration, urban enhancements, and uncertainty estimates, Atmos. Chem. Phys., 17, 8313–8341, https://doi.org/10.5194/acp-17-8313-2017, 2017.

Worden, H. M., Cheng, Y., Pfister, G., Carmichael, G. R., Zhang, Q., Streets, D. G.: Satellite-based estimates of reduced CO and CO_2 emissions due to traffic restrictions during the 2008 Beijing Olympics, *Geophysical Research Letters*, 39, 1–6, https://doi.org/10.1029/2012GL052395, 2012.

Xu, J., Lee, X., Xiao, W., Cao, C., Liu, S., Wen, X., Xu, J., Zhang, Z., and Zhao, J.: Interpreting the $^{13}C/^{12}C$ ratio of carbon dioxide in an urban airshed in the Yangtze River Delta, China, Atmos. Chem. Phys., 17, 3385–3399, https://doi.org/10.5194/acp-17-3385-2017, 2017.

Yang, Y., Wang, L., Cao, Z. Mou C., Shen, L.,Zhao, J.,and Fang, Y.: CO_2 emissions from cement industry in China: A bottom-up estimation from factory to regional and national levels. *Journal of Geographical Science,* 27, 711–730.

Zhao, C., Andrews, A. E., Bianco, L., Eluszkiewicz, J. Hirsh, A., Macdonald, C., Nehrkorn, T., and Fischer M. L.,. Atmospheric inverse estimates of methane emissions from Central California. *Journal of Geophysical Research*: *Atmospheres*, 2009, 114(D16): 4723-4734, https://doi.org/10.1029/2008JD011671, 2009.

Figure 1. (a) Weather Research and Forecasting Model simulation domains and the location of WLG site , the different region colors represent three domains, (b) cement production distribution in YRD and Eastern China. Both green dot in (a) and red star in (b) are NUIST observation site.

Figure 2. (a) Annual anthropogenic CO_2 emissions for study domain (units: mol m^{-2} s^{-1}) and population density in 4 megacities (units: people per hectare) including Nanjing, Hefei, Zhejiang, and Shanghai for the year of 2015, (b) Two-year average concentration footprint (units: ppm m^2 s/μmol).

Figure 3. (a) Comparisons of hourly CO_2 mixing ratios between observations and model simulation from September 2013 to August 2015, and monthly averages for (b) whole day, (c) nighttime (22:00-06:00, local time) and (d) daytime (10:00 - 16:00); Model results (red), observations (black), and background (grey).

Figure 4. Relation between monthly PBLH and change in CO_2 mixing ratio, here these dots represent difference of monthly averages in two different years for all hours.

Figure 5. (a) Comparisons of simulated and observed CO_2 enhancement, note 'model' represents the sum of both anthropogenic and biological CO_2 enhancement simulations, (b) CO_2 enhancement contributions from different provinces, (c) simulated anthropogenic CO_2 enhancement proportion for the main sources; Time series (2013 to 2015) of (d) NDVI, (e) SIF, and (f) GPP. The distance indicates the radius of area centered with NUIST observation site, and the NDVI, SIF, GPP values are averages in these areas.

Figure 6. Comparisons among three strategies for calculating the background $\boldsymbol{\delta}^{13}C\text{-}CO_2$. Strategy 1 (WLG discrete: weekly discrete observations at WLG site, WLG CCGCRV: derived hourly data with WLG observations and CCGCRV method); Strategy 2 (Calculated: by choosing clean air in winter); and strategy 3 (M-T method: derived results with observations and M-T approach, M-T CCGCRV: derived hourly results with M-T approach and CCGCRV method, see details in section 2.2.1).

Figure 7. (a) Comparisons of observed and modeled hourly $\boldsymbol{\delta}^{13}C\text{-}CO_2$ from September 2013 to August 2015, where the grey line represent derived $\boldsymbol{\delta}^{13}C\text{-}CO_2$ background, and (b) Simulated hourly biological CO_2 enhancement. The shade and lines in both subfigures represent the periods for winter and summer, respectively.

Figure 8. Comparisons of observed and modeled (a) CO_2 mixing ratio and (b) $\boldsymbol{\delta}^{13}C\text{-}CO_2$ from December 2013 to February 2014; (c) CO_2 mixing ratio and (b) $\boldsymbol{\delta}^{13}C\text{-}CO_2$ from December 2014 to February 2015; (e) CO_2 mixing ratio and (f) $\boldsymbol{\delta}^{13}C\text{-}CO_2$ from June 2014 to August 2014; (g) CO_2 mixing ratio and (h) $\boldsymbol{\delta}^{13}C\text{-}CO_2$ from June 2015 to August 2015.

Figure 9. Scatter plots of observed versus modeled (a) winter time CO_2 mixing ratios, (b) winter time $\boldsymbol{\delta}^{13}C\text{-}CO_2$, (c) summer time CO_2, and (d) summer time $\boldsymbol{\delta}^{13}C\text{-}CO_2$ for both years, here these dots are daily averages.

Figure 10. Digital filtering curve fitting (CCGCRV) for background, observations, normal simulations, case 1 (excluding negative NEE when photosynthesis is stronger than respiration), and case 2 (excluding respiration and photosynthesis) in both years, (b) $\boldsymbol{\delta}^{13}C\text{-}CO_2$ comparisons between normal simulations and case 1, and (c) $\boldsymbol{\delta}^{13}C\text{-}CO_2$ comparisons between normal simulations and case 2.

Figure 11. Comparisons of winter time $\boldsymbol{\delta}s\cdot\boldsymbol{\Delta}CO_2$ using (a) *a priori* and (b) constrained anthropogenic CO_2 emissions.

Figure 12. (a) Comparisons between observed and modeled $\boldsymbol{\delta}_s$, (b) relationship between cement CO_2 enhancement proportion and simulated anthropogenic $\boldsymbol{\delta}s$ for nighttime and (c) all-day.

Figure 13. Sensitivity tests showing the influence of cement CO_2 emissions on $\boldsymbol{\delta}_s$ for (a) nighttime, (b) all-day, and (c) the relation between cement CO_2 and $\boldsymbol{\delta}^{13}C$ for simulation strategies 1 (There is no bias in the total anthropogenic CO_2 enhancement such that a proportional increase/decrease in the cement component does not change the relative anthropogenic contributions) and 2 (only the cement enhancement changes). Note that the numbers in brackets indicate changes in $\boldsymbol{\delta}^{13}C$ with cement CO_2

enhancement proportion (the fraction of cement CO_2 enhancement to simulated total CO_2 enhancement) increase by 0.2 times. The x-axis values indicate changing cement enhancement proportions to 0.8 1.2, 1.4, 1.6, 1.8, and 2 times the original values.

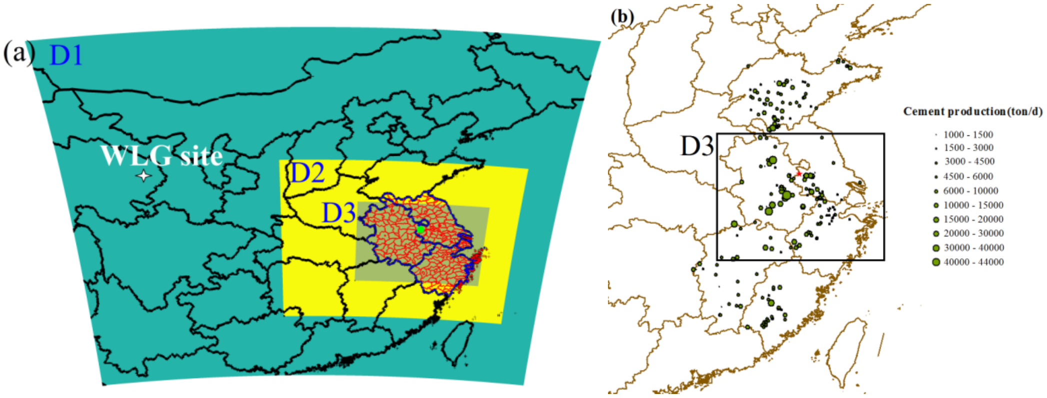

Figure 1. (a) Weather Research and Forecasting Model simulation domains and the location of WLG site , the different region colors represent three domains, (b) cement production distribution in YRD and Eastern China. Both green dot in (a) and red star in (b) are NUIST observation site.

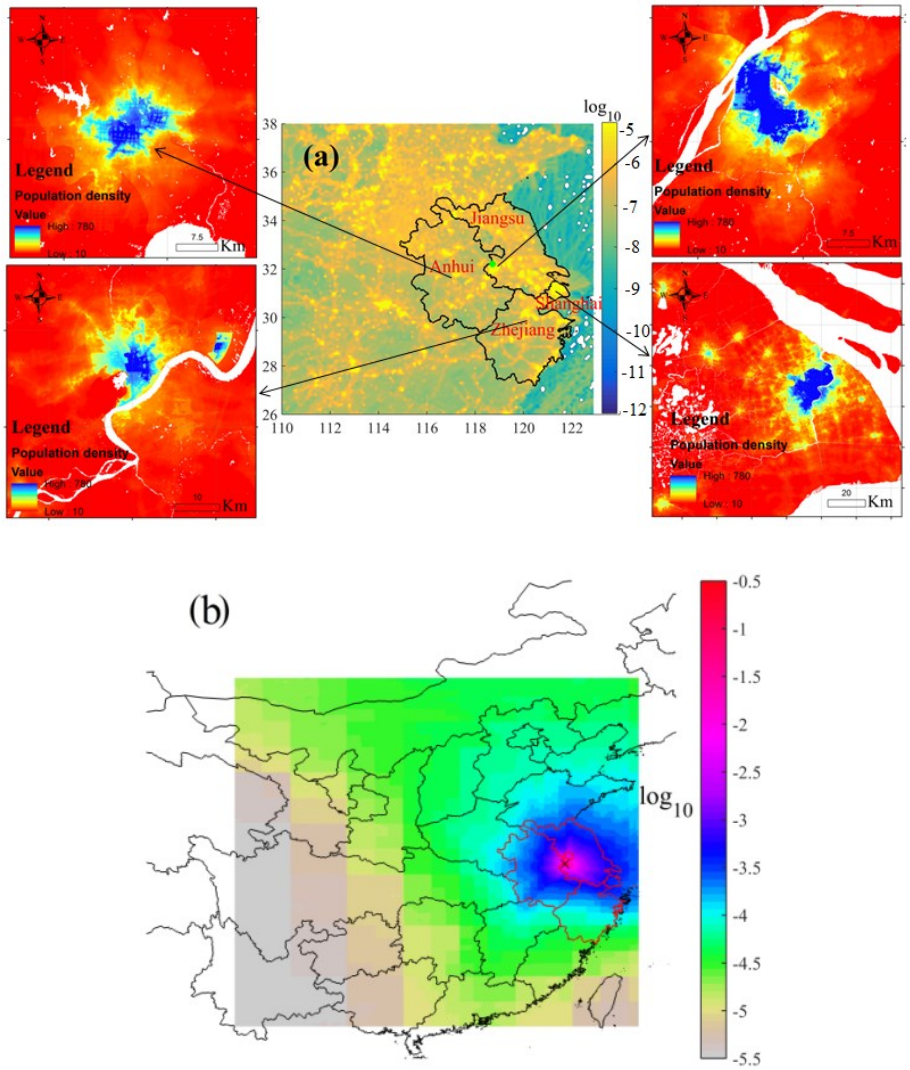

Figure 2. (a) Annual anthropogenic CO_2 emissions for study domain (units: mol m^{-2} s^{-1}) and population density in 4 megacities (units: people per hectare) including Nanjing, Hefei, Zhejiang, and Shanghai for the year of 2015, (b) Two-year average concentration footprint (units: ppm m^2 s/μmol).

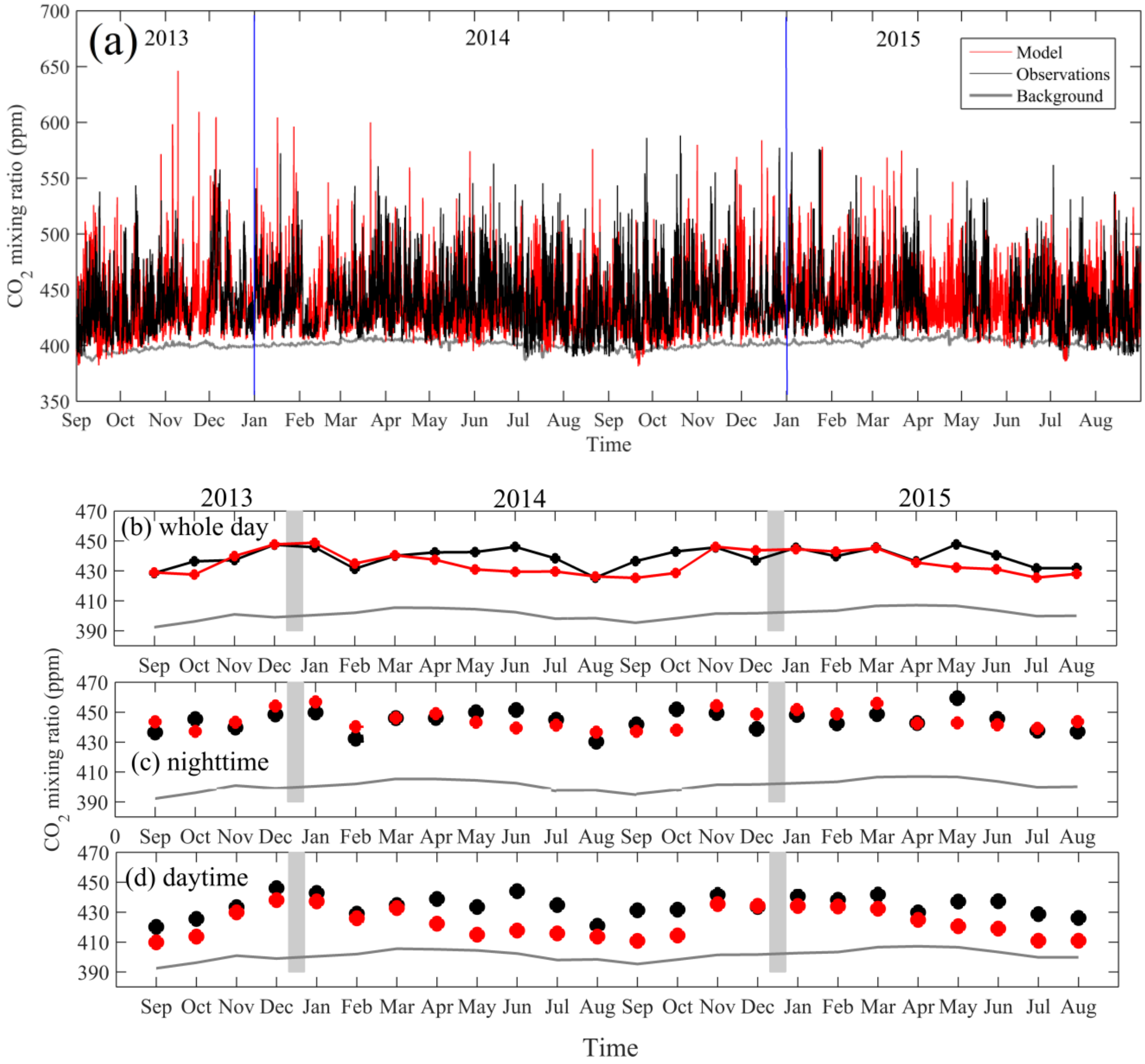

Figure 3. (a) Comparisons of hourly CO_2 mixing ratios between observations and model simulation from September 2013 to August 2015, and monthly averages for (b) whole day, (c) nighttime (22:00-06:00, local time) and (d) daytime (10:00 - 16:00); Model results (red), observations (black), and background (grey).

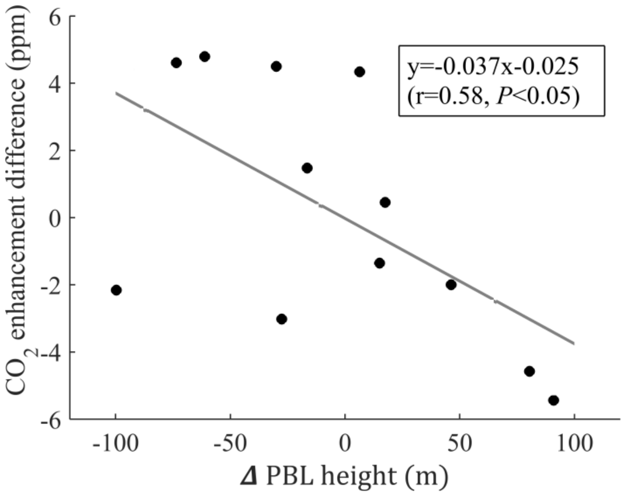

Figure 4. Relation between monthly PBL height and change in CO_2 mixing ratio, here these dots represent difference of monthly averages in two different years for all hours.

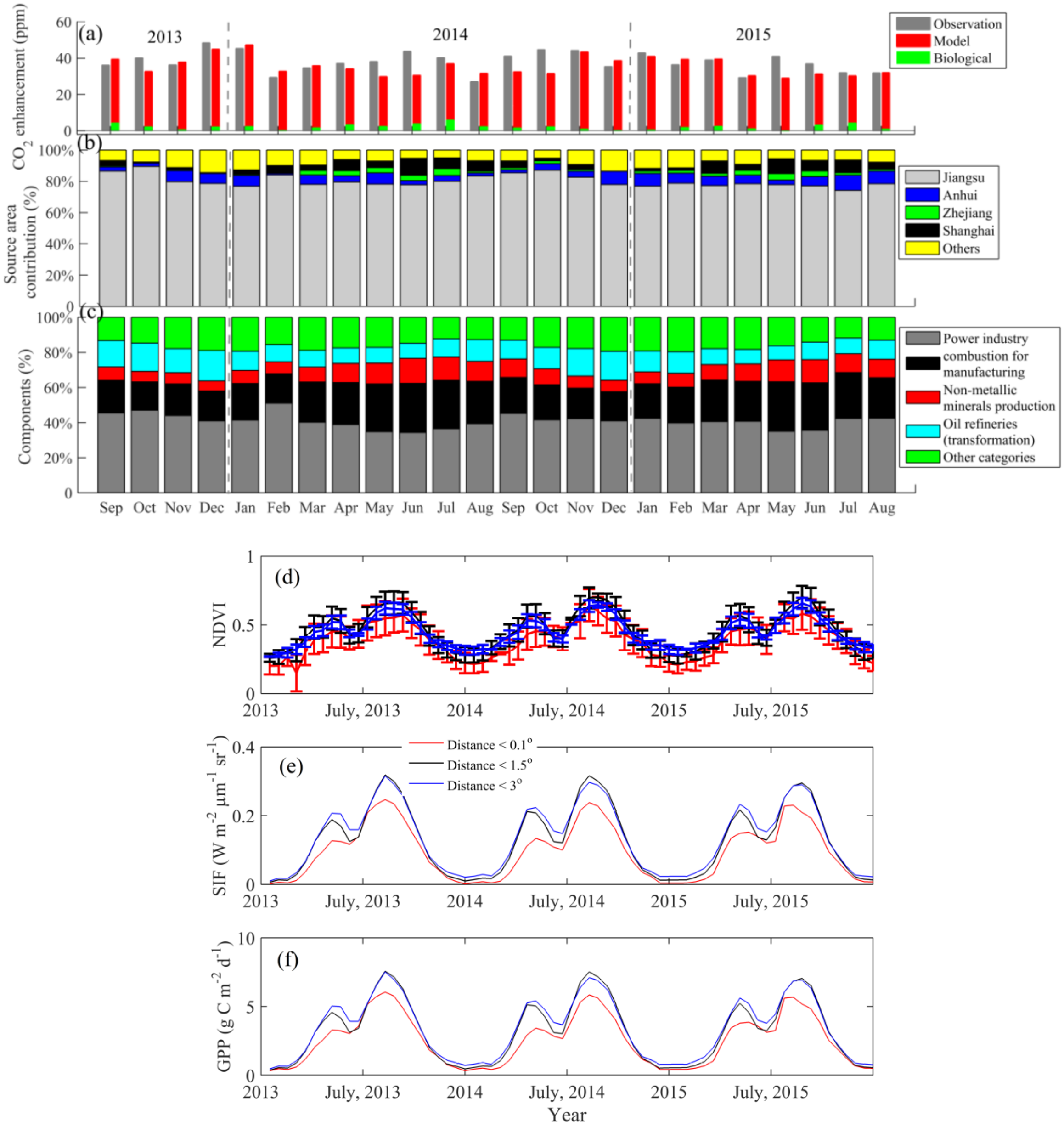

Figure 5. (a) Comparisons of simulated and observed CO_2 enhancement, note 'model' represents the sum of both anthropogenic and biological CO_2 enhancement simulations, (b) CO_2 enhancement contributions from different provinces, (c) simulated anthropogenic CO_2 enhancement proportion for the main sources; Time series (2013 to 2015) of (d) NDVI, (e) SIF, and (f) GPP. The distance indicates the radius of area centered with NUIST observation site, and the NDVI, SIF, GPP values are averages in these areas.

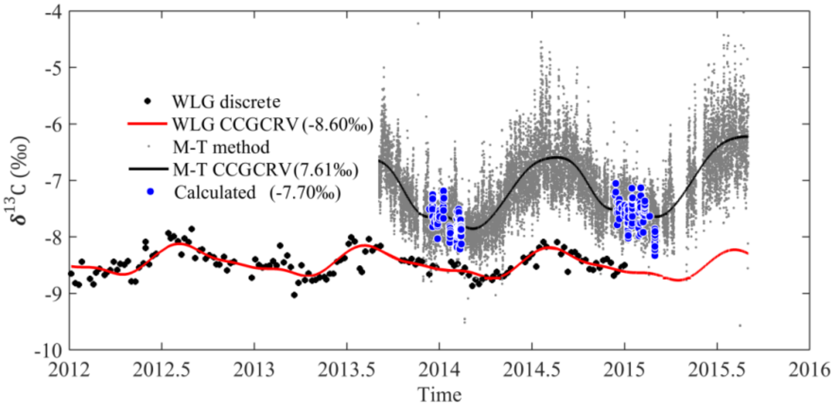

Figure 6. Comparisons among three strategies for calculating the background δ^{13}C-CO$_2$. Strategy 1 (WLG discrete: weekly discrete observations at WLG site, WLG CCGCRV: derived hourly data with WLG observations and CCGCRV method); Strategy 2 (Calculated: by choosing clean air in winter); and strategy 3 (M-T method: derived results with observations and M-T approach, M-T CCGCRV: derived hourly results with M-T approach and CCGCRV method, see details in section 2.2.1).

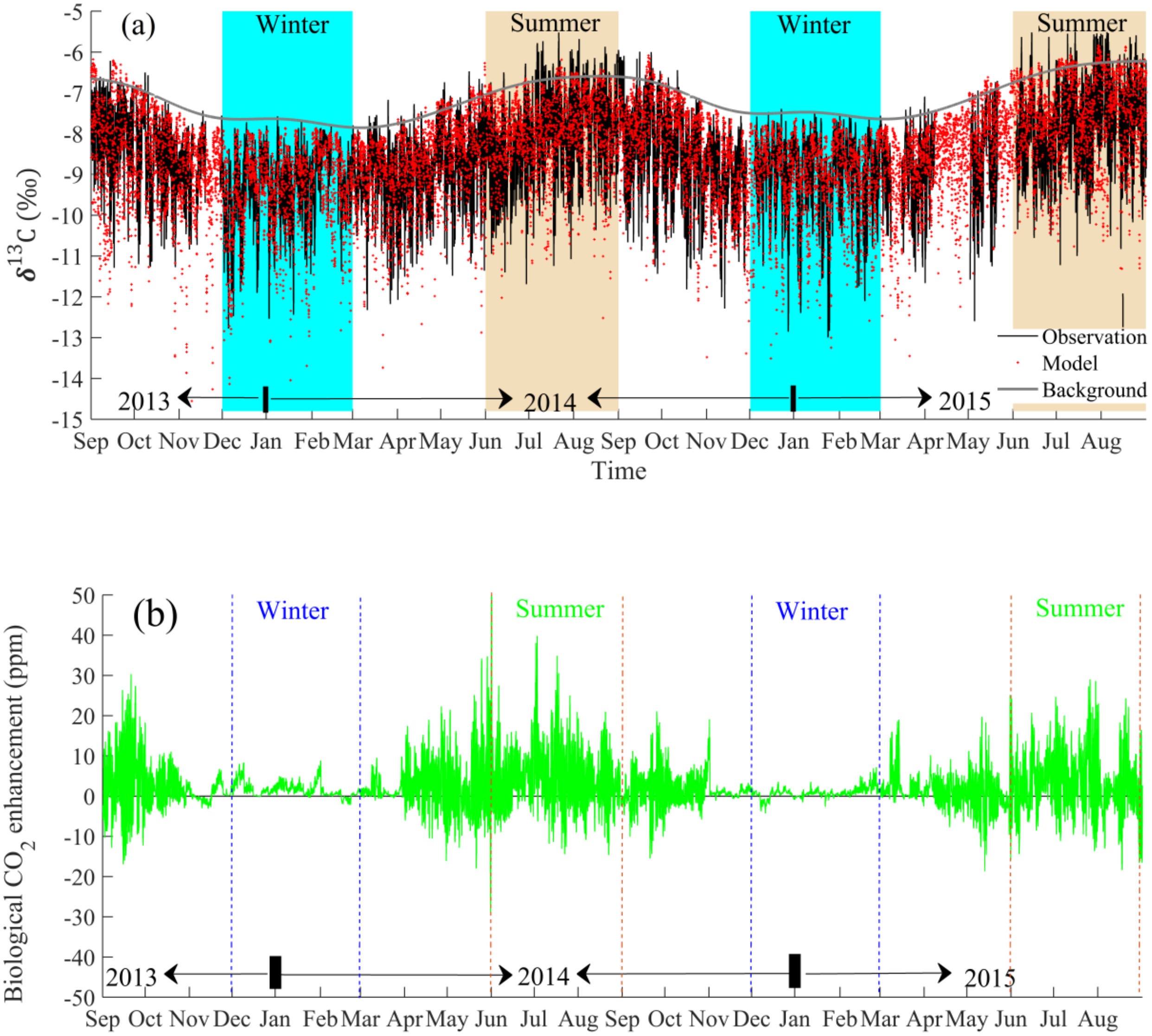

Figure 7. (a) Comparisons of observed and modeled hourly δ^{13}C-CO$_2$ from September 2013 to August 2015, where the grey line represent derived δ^{13}C-CO$_2$ background, and (b) Simulated hourly biological CO$_2$ enhancement. The shade and lines in both subfigures represent the periods for winter and summer, respectively.

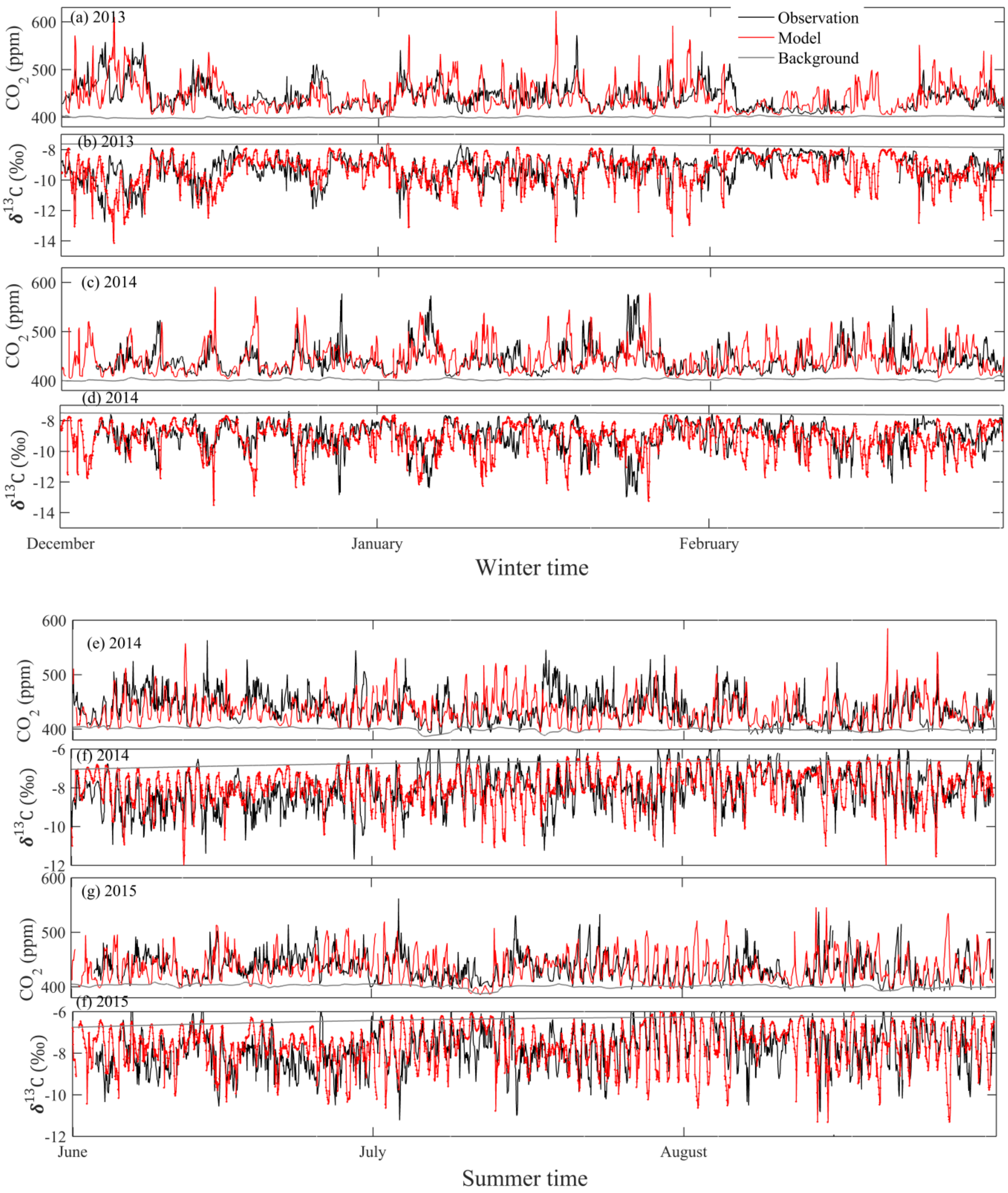

Figure 8. Comparisons of observed and modeled (a) CO$_2$ mixing ratio and (b) $\boldsymbol{\delta}^{13}$C-CO$_2$ from December 2013 to February 2014; (c) CO$_2$ mixing ratio and (b) $\boldsymbol{\delta}^{13}$C-CO$_2$ from December 2014 to February 2015; (e) CO$_2$ mixing ratio and (f) $\boldsymbol{\delta}^{13}$C-CO$_2$ from June 2014 to August 2014; (g) CO$_2$ mixing ratio and (h) $\boldsymbol{\delta}^{13}$C-CO$_2$ from June 2015 to August 2015.

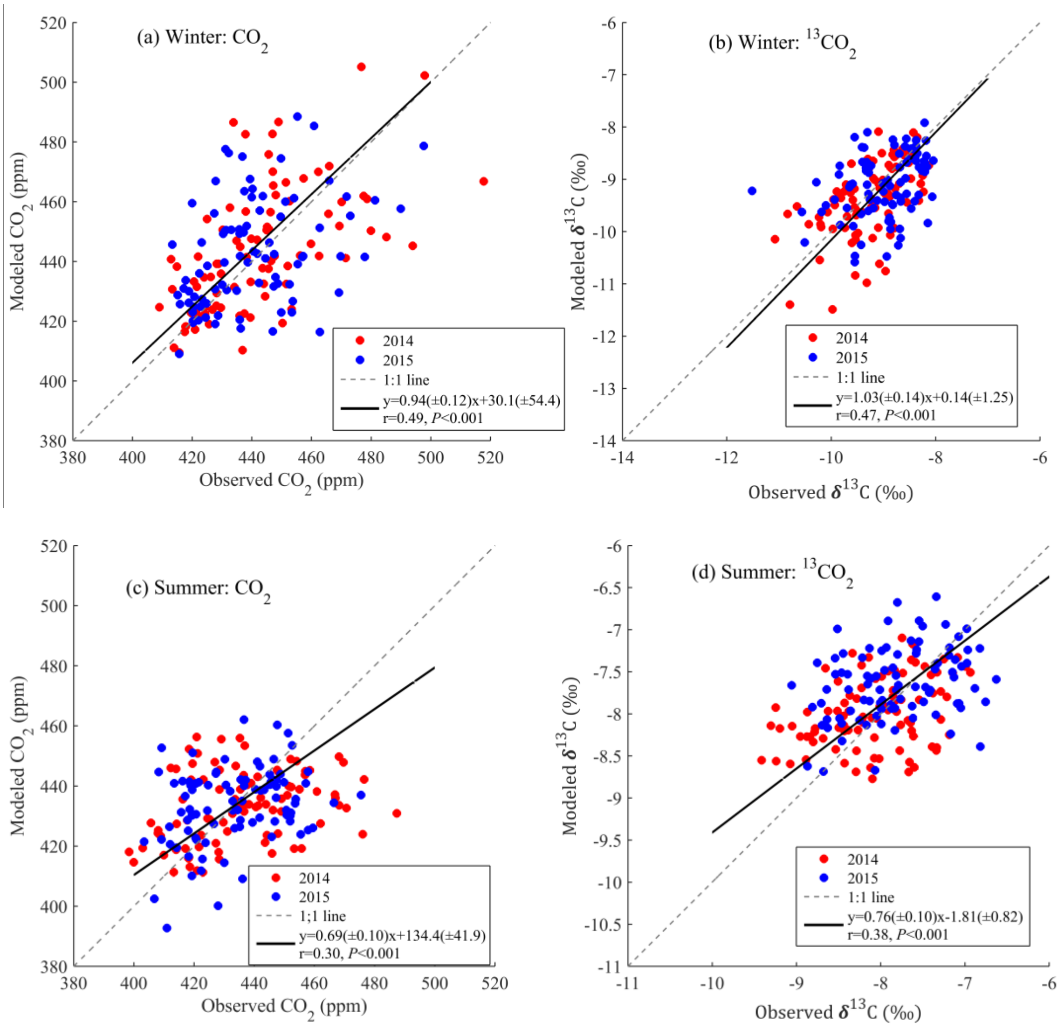

Figure 9. Scatter plots of observed versus modeled (a) winter time CO_2 mixing ratios, (b) winter time $\delta^{13}C$-CO_2, (c) summer time CO_2, and (d) summer time $\delta^{13}C$-CO_2 for both years, here these dots are daily averages.

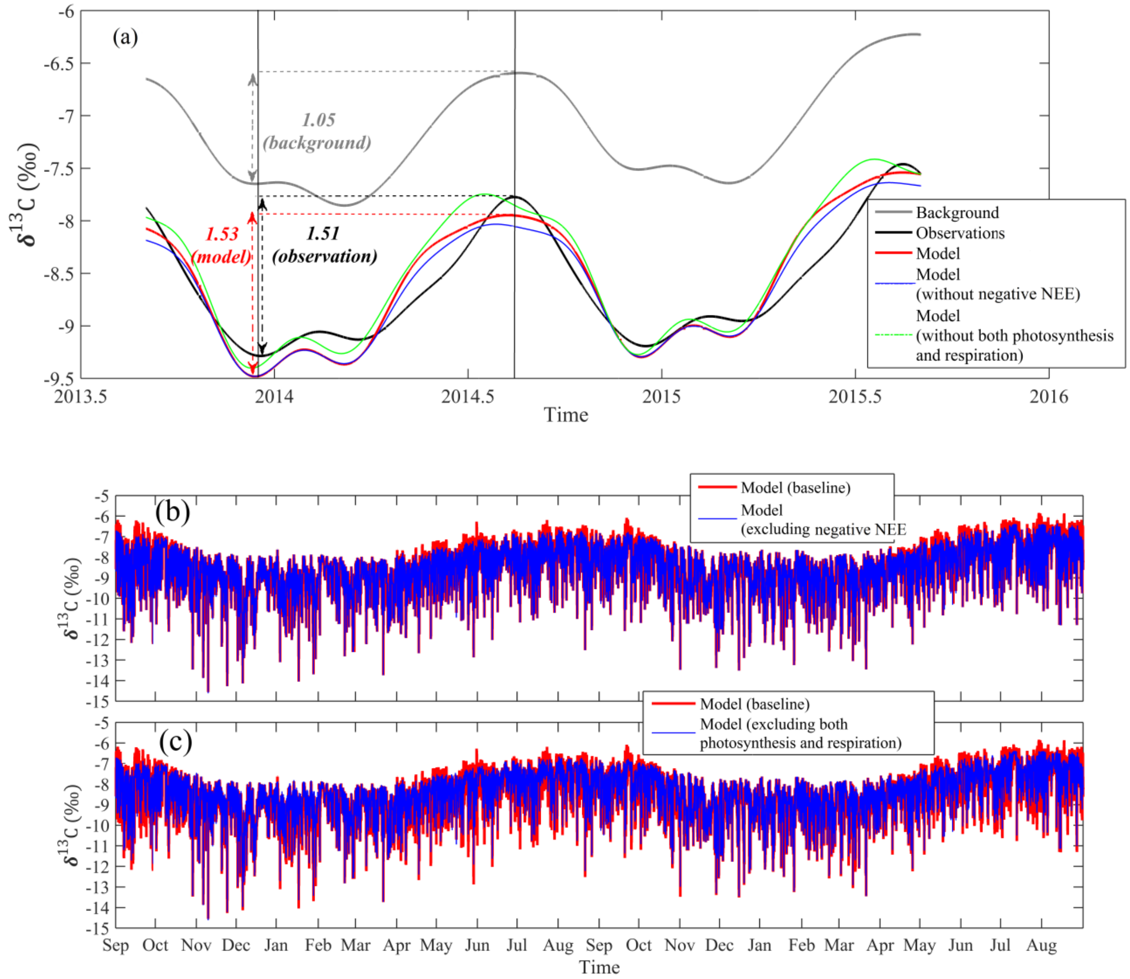

Figure 10. Digital filtering curve fitting (CCGCRV) for background, observations, normal simulations, case 1 (excluding negative NEE when photosynthesis is stronger than respiration), and case 2 (excluding respiration and photosynthesis) in both years, (b) $\boldsymbol{\delta}^{13}$C-CO$_2$ comparisons between normal simulations and case 1, and (c) $\boldsymbol{\delta}^{13}$C-CO$_2$ comparisons between normal simulations and case 2.

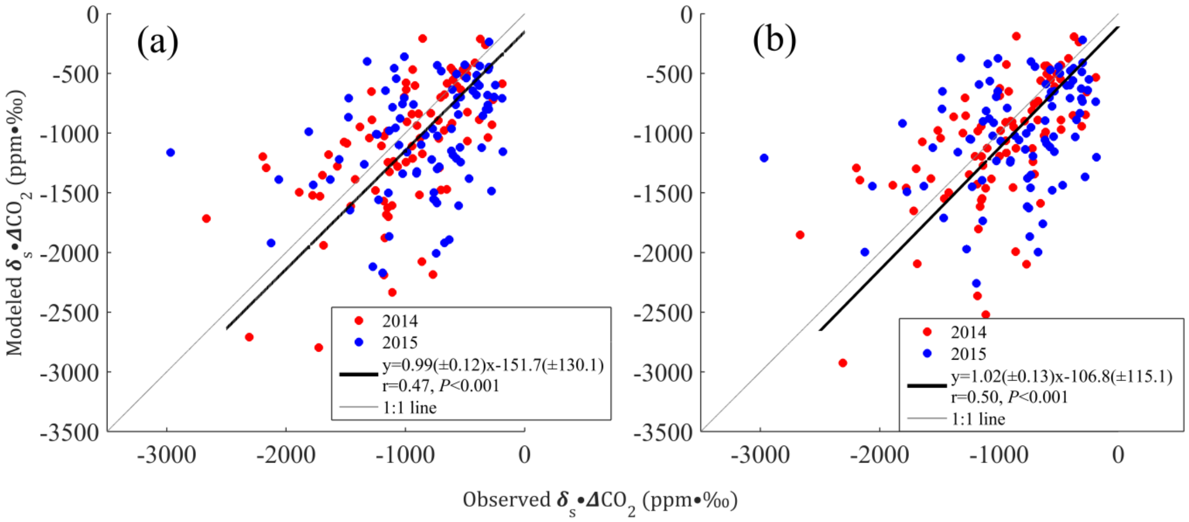

Figure 11. Comparisons of winter time $\boldsymbol{\delta}$s·$\boldsymbol{\Delta}CO_2$ using (a) *a priori* and (b) constrained anthropogenic CO_2 emissions.

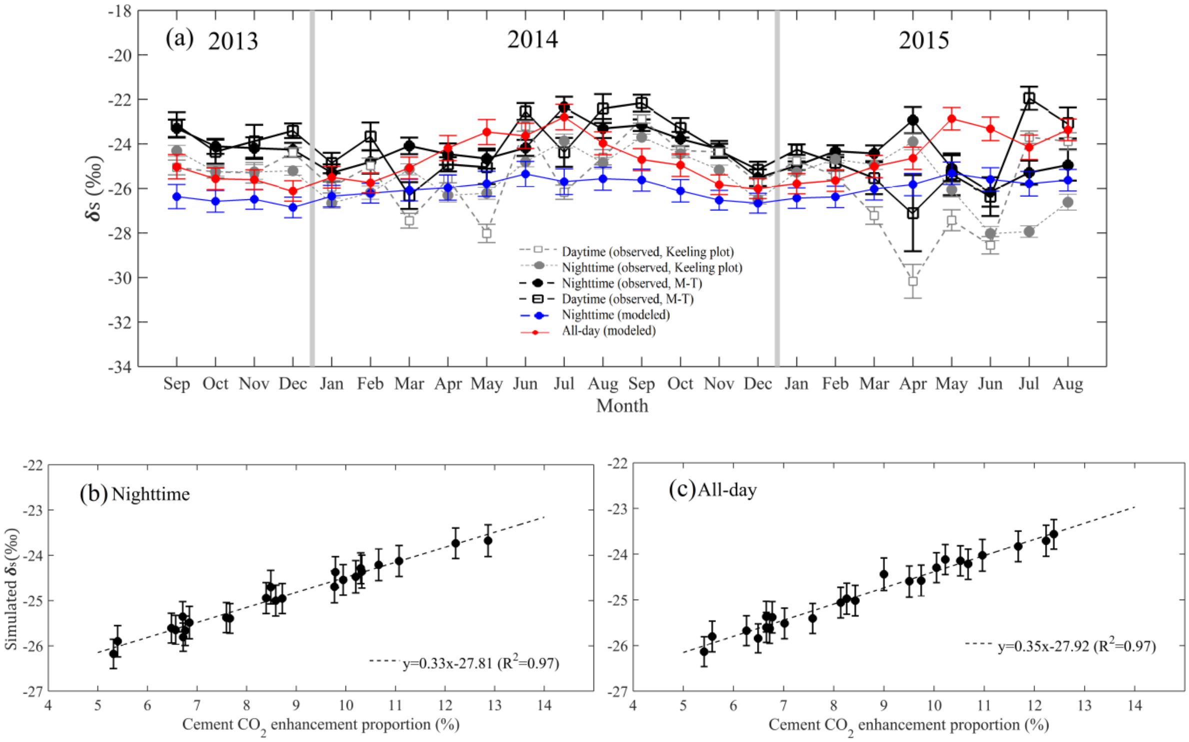

Figure 12. (a) Comparisons between observed and modeled $\boldsymbol{\delta}_{s}$, (b) relationship between cement CO_2 enhancement proportion and simulated anthropogenic $\boldsymbol{\delta}$s for nighttime and (c) all-day.

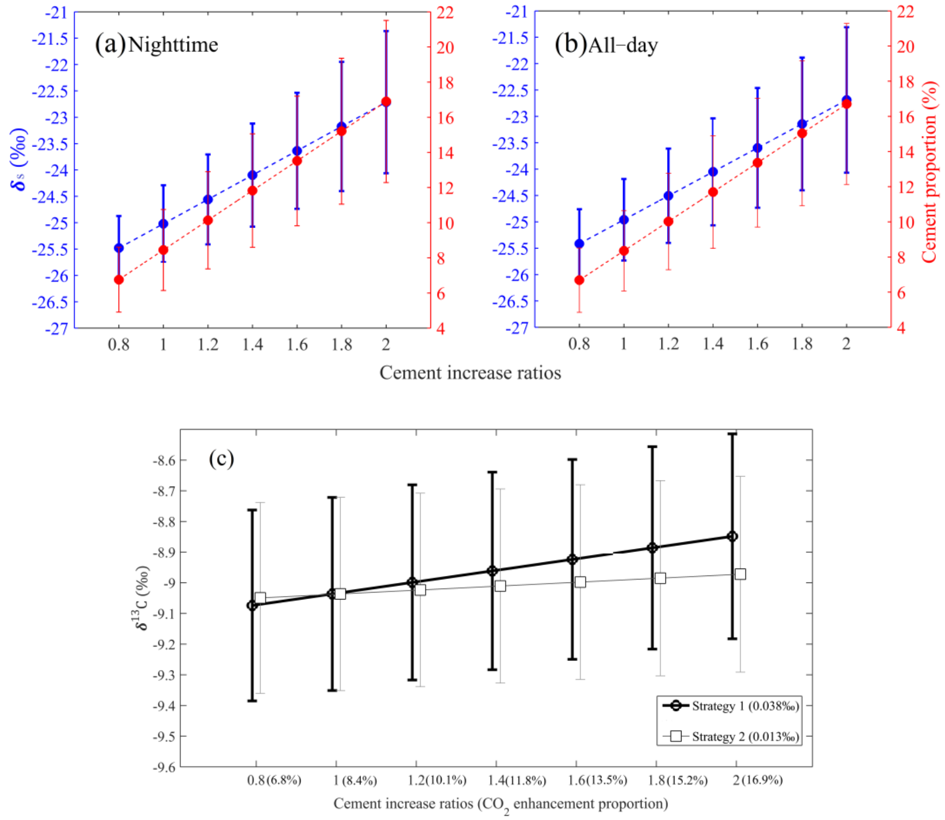

Figure 13. Sensitivity tests showing the influence of cement CO_2 emissions on $\boldsymbol{\delta}_s$ for (a) nighttime, (b) all-day, and (c) the relation between cement CO_2 and $\boldsymbol{\delta}^{13}$C for simulation strategies 1 (There is no bias in the total anthropogenic CO_2 enhancement such that a proportional increase/decrease in the cement component does not change the relative anthropogenic contributions) and 2 (only the cement enhancement changes). Note that the numbers in brackets indicate changes in $\boldsymbol{\delta}^{13}$C with cement CO_2 enhancement proportion (the fraction of cement CO_2 enhancement to simulated total CO_2 enhancement) increase by 0.2 times. The x-axis values indicate changing cement enhancement proportions to 0.8 1.2, 1.4, 1.6, 1.8, and 2 times the original values.

Table 1. Comparisons of cement and all anthropogenic CO_2 emissions among different methods, "/" means not available.

Units: × 10^{11} kg	Year	EDGAR v432	Inversion results	IPCC method
Cement CO_2 emissions	2010	1.45	/	1.14
	2014-2015	1.72	/	1.35
All anthropogenic CO_2 emissions	2010	20.55	/	17.56
	2014-2015	23.53	24.59±2.39	24.38

Table 2. Statistical metrics between observed and modeled CO$_2$ mixing ratios and $\boldsymbol{\delta}^{13}$C-CO$_2$ during winter, summer and annual for 2014 and 2015. Correlation coefficient (R), averages and root mean square error (RMSE) are displayed.

	Years	2014			2015		
	Periods	allyear	Winter	Summer	allyear	Winter	Summer
$\boldsymbol{\delta}^{13}CO_2$ (‰)	R	0.54	0.40	0.47	0.52	0.27	0.39
	RMSE (‰)	1.07	0.94	0.94	1.10	0.92	0.98
	simulation (‰)	-8.68	-9.37	-8.02	-8.45	-9.10	-7.66
	observation (‰)	-8.69	-9.27	-8.09	-8.52	-8.98	-7.83
CO_2	R	0.38	0.41	0.34	0.35	0.28	0.31
	RMSE (ppm)	29.44	27.48	25.55	30.22	26.81	24.29
	simulation (ppm)	436.47	441.55	436.67	437.08	442.09	432.37
	observation (ppm)	438.49	442.03	432.25	440.11	440.77	434.71